

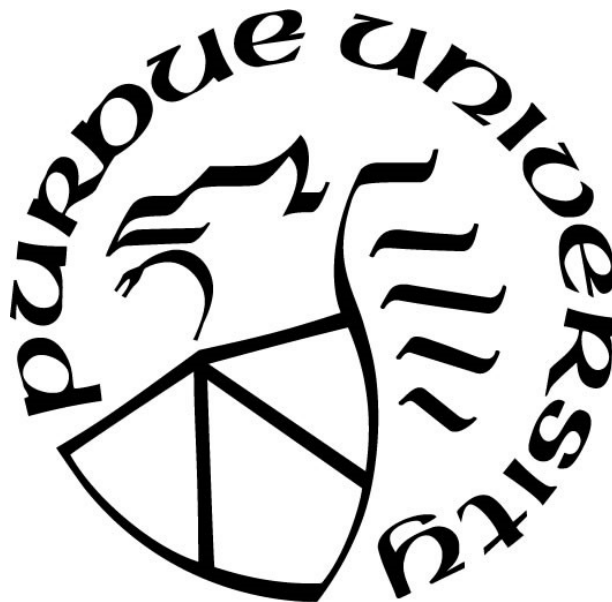
**HIGH-THROUGHPUT CALCULATIONS AND EXPERIMENTATION
FOR THE DISCOVERY OF REFRACTORY COMPLEX
CONCENTRATED ALLOYS WITH HIGH HARDNESS**

by
Austin Hernandez

A Thesis

*Submitted to the Faculty of Purdue University
In Partial Fulfillment of the Requirements for the degree of*

Master of Science in Materials Engineering



School of Materials Engineering
West Lafayette, Indiana
May 2022

THE PURDUE UNIVERSITY GRADUATE SCHOOL
STATEMENT OF COMMITTEE APPROVAL

Dr. Kenneth H. Sandhage, Co-Chair

School of Materials Engineering

Dr. Michael S. Titus, Co-Chair

School of Materials Engineering

Dr. Alejandro Strachan

School of Materials Engineering

Dr. Janelle Wharry

School of Materials Engineering

Approved by:

Dr. David F. Bahr

To my parents, Antonio Hernandez Jr and Corina Hernandez
And to my love, Audrey Doughty

ACKNOWLEDGMENTS

I would like to thank my committee for their extremely helpful guidance throughout my graduate school journey, and especially my co-advisors, Dr. Titus and Dr. Sandhage for their never-ending patience and support. I would also like to thank everyone at Kepner laboratories and from my research group that has assisted me in any way, namely Dr. Mario Caccia, Yujie Wang, Adam Caldwell, Alex Strayer, Sona Avetian, Priyatham Tumurugoti, Camilla McCormack, Caleb Schrad, Tom Mann, Glenn Peterson, Saeid Kakooei, Pavan Srivas, Sunghwan Hwang, Dr. Dongsheng Wen and many others. I am also extremely grateful for the help of Sharmila Karumuri, Zack McClure, and Saswat Misra for their expertise in data science and machine learning as this project would not be possible without them.

I am also eternally grateful for my family, who has supported me throughout my academic career, and especially my grandparents for always worrying about me and cheering me on, and my dad for always encouraging me to strive for greatness.

Finally, I am extremely grateful for the love of my life, Audrey, for her unwavering support and encouragement, no matter how many nights I work late and her constant effort to see the positive side of everything.

TABLE OF CONTENTS

LIST OF TABLES	7
LIST OF FIGURES	8
ABSTRACT.....	11
1. INTRODUCTION	13
2. A CALPHAD-BASED APPROACH TO DESIGN REFRACTORY CONCENTRATED COMPLEX ALLOYS CAPABLE OF FORMING A CONTINUOUS Al_2O_3 PROTECTIVE SCALE UPON OXIDATION AT 1000 °C	19
2.1 Introduction.....	19
2.2 Construction of Initial Compositional Design Space	20
2.3 Computational Methods: Scripts Created for the Down-Selection of a Grid of Alloys ...	21
2.3.1 Get_phases_and_structures.....	21
2.3.2 Try_calculating_solvus.....	22
2.3.3 Get_fabrication_method	23
2.4 Results and Discussion	25
2.5 Conclusions.....	32
3. HIGH-THROUGHPUT EXPERIMENTATION FOR THE DISCOVERY OF HIGH STRENGTH ALLOYS BY ACTIVE LEARNING	33
3.1 Introduction.....	33
3.2 Methods.....	37
3.2.1 Method of Alloy Selection: Active Learning Using Bayesian Global Optimization	37
3.2.2 Experimental Methods.....	40
<i>Alloy Fabrication Methods</i>	40
<i>Post-Fabrication Sample Preparation</i>	42
<i>Sample Characterization</i>	43
3.3 Results and Discussion	44
3.3.1 1 st Iteration of Active Learning.....	44
3.3.2 2 nd Iteration of Active Learning.....	47
3.3.3 3 rd Iteration of Active Learning	50

3.3.4	4 th Iteration of Active Learning	53
3.3.5	5 th and final Iteration of Active Learning	56
3.3.6	Review of All Active Learning Iterations	59
3.3.7	Experimental and Theoretical Yield Strength	62
3.4	Conclusions.....	65
4.	CONCLUDING REMARKS AND FUTURE WORK.....	67
	APPENDIX.....	68
	REFERENCES	71

LIST OF TABLES

Table 2-1 Comparison of compositions with minimum and maximum optimized values.	29
Table 3-1 Data for 1 st round of active learning.	46
Table 3-2 Data for 2 nd round of active learning.	49
Table 3-3 Data for 3 rd round of active learning.	52
Table 3-4 Data for 4 th round of active learning.	55
Table 3-5 Data for 5 th round of active learning	58
Table 4-1. The compositions, lattice parameters, predicted shear strength found from the Curtin model, yield strength found by multiplying by a Taylor factor of 2.75 for BCC polycrystals, GP model predictions, and experimental yield strength, if measured for AL alloys.	70

LIST OF FIGURES

Figure 1-1. Ashby plot showing Ni-based superalloys in the orange region and comparing their high temperature strength to recent works involving RCCAs. Adapted from Ref. [14].	15
Figure 1-2. Mass gain versus time curve of NV1 at 1100 °C and a total time of 200 hours. This result shows unprecedented oxidation resistance of an RCCA when compared to other RCCAs previously reported. Figure adapted from Ref. [15].	16
Figure 1-3. a) Hardness parity plot of predicted hardness values and their accuracy when compared to the initial training set. b) Results of active learning loop and differences when using property plus composition (Loop I) versus composition plus knowledge. Adapted from Ref. [21].	17
Figure 1-4. A plot showing the mass gain over area versus a specific strength. Ni-based superalloys currently provide superior oxidation resistance than any RCCA, but there are some RCCAs with a higher specific strength. The target property space is a specific strength of 70 MPa cm ³ /g and a mass gain of 1 mg/cm ²	18
Figure 2-1 The elemental palette considered. It consisted of the 9 refractory elements (Ti, Zr, Hf, V, Nb, Ta, Cr, Mo, and W) plus Al for oxidation resistance. Adapted from Ref. [9].	21
Figure 2-2 a) A graphical representation of the boiling point issue when melting volatile elements such as Al and Cr with high melting point elements such as Mo and W. The <code>get_fabrication_method</code> function aimed to solve this issue. b) An attempt at arc melting a CrMoW alloy that underwent significant Cr vaporization and formation of large pores.	24
Figure 2-3 . a) 3D color mapping of the initial design space. b)t-SNE plot with ideal mixing entropy plotted with a greyscale.	25
Figure 2-4 a) All alloys that are single phase and possess a BCC solvus temperature lower than 1000 °C. b) Powder processing alloys. c) Arc meltable alloys.	26
Figure 2-5 The frequency of elements in the compositions of both fabrication methods. Elements with some solubility at high temperature with Al (V, Nb, Mo, Ti) show a good number of single phase compositions, and those that readily form intermetallic compounds (Cr, Zr, Hf, and Ta) are low in quantity.	27
Figure 2-6 a) Multi-objective optimization plot and Pareto front for arc melt-able alloys. b) Multi-objective optimization plot and pareto front for powder processing alloys. c) Quantity of systems that lie on the Pareto front of arc melt-able alloys. d) Quantity of systems that lie on the Pareto front of powder processing alloys.	28
Figure 2-7 Correlation heatmap between the predicted hardness of all single-phase arc meltable alloys.	30
Figure 2-8 Correlation heatmap between the predicted hardness of all single-phase powder processing alloys.	31
Figure 3-1 The proposed machine learning accelerated materials discovery framework that combines machine learning, ab initio simulations, high-throughput (low-fidelity) and full-scale	

(high-fidelity) experiments. Target metrics are a low mass gain in oxidizing environments and high strength. From NSF DMREF proposal	34
Figure 3-2 A simplistic schematic of the active learning procedure, and a similar process is followed in the present work. Adapted from Ref. [25].	35
Figure 3-3. a) A comparison between RT yield strength and grain size of different processing methods. b) An analysis of the Vickers hardness and room temperature strength of both multi- and single-phase alloys from the HEA dataset.	36
Figure 3-4. Visualization of the number of alloys with hardness data that belong in each design space. By reducing the dimensionality of the design space, it is revealed that there is a large gap in knowledge of strength for single phase, Al-bearing, 4-component RCCAs.	36
Figure 3-5. A flow chart summarizing the Bayesian Global Optimization process. This figure is credited to Sharmila Karumuri and Ilias Bilonis.	38
Figure 3-6. The amended BGO process showing the primary differences from a regular BGO process. The model assumed the experimental data was equal to the predicted hardness, which was then fed back into itself to compute a new maximum EI value for identifying the next alloys. This figure is credited to Sharmila Karumuri and Ilias Bilonis.	39
Figure 3-7. A workflow detailing the process from a grid of alloys potential RCCAs to a list of experiments, with the active learning loop a critical step in discovering novel alloy properties.	40
Figure 3-8 A typical ingot shape after fabrication. The shape, presence of a shrinkage cavity, and luster of the final product is relevant for data storage purposes.	42
Figure 3-9. Results of HV testing compared to predictions for round 1 of active learning. b) XRD scans showing single set of BCC peaks for all alloys in round 1.	44
Figure 3-10. Polished micrographs taken with BSE imaging in the 1 st round of active learning. Most of the alloys appear to have chemical microsegregation.	45
Figure 3-11 Hardness parity plot showing results of 1st round and comparison with literature data.	45
Figure 3-12. HV and XRD results for 2 nd round of active learning. All alloys are harder than the benchmark, and the XRD scans only show 1 set of BCC peaks.....	47
Figure 3-13. Polished micrographs taken with BSE imaging in the 2 nd round of active learning.....	48
Figure 3-14 Hardness parity plot of the 2 nd round which shows little agreement with the experimental hardness values.	48
Figure 3-15 HV results and XRD scans for 3 rd round of active learning	50
Figure 3-16. Polished micrographs taken with BSE imaging in the 3 rd round of active learning.....	51
Figure 3-17. Hardness parity plot of the 3 rd round showing excellent agreement with measured values.	51
Figure 3-18. HV results and XRD scans for the 4 th round of active learning.....	53

Figure 3-19. Polished micrographs taken with BSE imaging in the 4 th round of active learning. Most of the alloys appear to have chemical microsegregation, except for 4.2.	54
Figure 3-20. Hardness parity plot of the 4 th round showing excellent agreement with the line of linear fit.	54
Figure 3-21 HV and XRD data from final round of active learning. Last alloy tested is the hardest out of all alloys tested in this loop.	56
Figure 3-22. Polished micrographs taken with BSE imaging in the 5 th round of active learning. All the alloys appear to exhibit chemical microsegregation.	57
Figure 3-23 Hardness parity plot of the 5 th round of active learning. Model appears to predict extremely HV well after only 5 iterations.	57
Figure 3-24 a) Compilation of XRD scans for all active learning alloys. b) Comparison of each iteration to the previous round and to literature values. Maximum is CrNbTiW with an HV of 630. c) Convergence of hardness predictions versus experimental values.	59
Figure 3-25 Plotting hardness versus at% of elements present in AL loop. No obvious trends are observed through these comparisons.	60
Figure 3-26. Compilation of hardness results from all iterations. Benchmark of AlMoNbTi is shown to have been passed by 15 alloys.	61
Figure 3-27. Correlation mapping of hardness versus composition and other thermodynamic properties.	62
Figure 3-28. Stress strain curve of the strongest alloy evaluated by compression testing. The peak stress is recorded at the point of yielding and is circled.	63
Figure 3-29. The RT yield strength comparisons of different categories of CCAs found in the literature. The three AL alloys tested are on the right-most column, and it is seen that a slight improvement over AlNbTaTi (YS: 1152 MPa) was accomplished.	63
Figure 3-30. The predicted yield stresses at room temperature and 1000 °C are compared, and the experimental results are also shown in the plot. The actual yield strength of the three alloys show some agreement with the predicted values, and there the Al ₆ -Hf ₄₁ -Mo ₂₉ -Nb ₂₄ exhibits anomalous high strength at both temperatures. Credit for DFT calculations goes to Dr. Dongsheng Wen and the GP model to Sharmila Karumuri.	64

ABSTRACT

Ni-based superalloys continue to exert themselves as the industry standards in high stress and highly corrosive/oxidizing environments, such as are present in a gas turbine engine, due to their excellent high temperature strengths, thermal and microstructural stabilities, and oxidation and creep resistances. Gas turbine engines are essential components for energy generation and propulsion in the modern age. However, Ni-based superalloys are reaching their limits in the operating conditions of these engines due to their melting onset temperatures, which is approximately 1300 °C. Therefore, a new class of materials must be formulated to surpass the capabilities Ni-based superalloys, as increasing the operating temperature leads to increased efficiency and reductions in fuel consumption and greenhouse gas emissions. One of the proposed classes of materials is termed refractory complex concentrated alloys, or RCCAs, which consist of 4 or more refractory elements (in this study, selected from: Ti, Zr, Hf, V, Nb, Ta, Cr, Mo, and W) in equimolar or near-equimolar proportions. So far, there have been highly promising results with these alloys, including far higher melting points than Ni-based superalloys and outstanding high-temperature strengths in non-oxidizing environments. However, improvements in room temperature ductility and high-temperature oxidation resistance are still needed for RCCAs. Also, given the millions of possible alloy compositions spanning various combinations and concentrations of refractory elements, more efficient methods than just serial experimental trials are needed for identifying RCCAs with desired properties. A coupled computational and experimental approach for exploring a wide range of alloy systems and compositions is crucial for accelerating the discovery of RCCAs that may be capable of replacing Ni-based superalloys.

In this thesis, the CALPHAD method was utilized to generate basic thermodynamic properties of approximately 67,000 Al-bearing RCCAs. The alloys were then down-selected on the basis of certain criteria, including solidus temperature, volume percent BCC phase, and aluminum activity. Machine learning models with physics-based descriptors were used to select several BCC-based alloys for fabrication and characterization, and an active learning loop was employed to aid in rapid alloy discovery for high hardness and strength. This method resulted in rapid identification of 15 BCC-based, four component, Al-bearing RCCAs exhibiting room-temperature Vickers hardness from 1% to 35% above previously reported alloys. This work exemplifies the advantages

of utilizing Integrated Computational Materials Engineering- and Materials Genome Initiative-driven approaches for the discovery and design of new materials with attractive properties.

1. INTRODUCTION

The electrical energy required to sustain the growing global population must meet ever-increasing demands. One of the most well-known and highly-studied methods for electricity generation involves the use of gas turbine engines. Hundreds of hours of sustained, high temperature operation are required for gas turbine engines. Such engines require the use of materials with a combination of high temperature and fatigue strength, creep and oxidation resistance, fracture toughness, and microstructural and thermal stability^{1,2}. To date, Ni-based superalloys have answered this demand and are capable of operating at about 70% of their melting points, or between 900 and 1100 °C, for long periods of time in harsh environments, unlike other alloy classes. To accomplish this engineering feat, thousands of engineers for over 70 years contributed to designing, testing, characterizing, and implementing these alloys with marked improvement over the decades³. Through fine tuning of processing and manufacturing controls and improvements such as directional and single crystal casting, the lifespans of Ni-based alloys have remarkably quadrupled since the early days of superalloys.² Another feature of Ni-based superalloys that allows for sustained operation in highly oxidizing environments is the formation of a protective α -Al₂O₃ scale on the alloy surface.^{4,5}

As previously mentioned, the energy requirements for modern society have risen significantly, and turbine engines must also improve their operating temperatures to match this demand. It is well known that increasing the peak operating temperature of an engine can improve engine efficiency for enhanced electricity production and reduced greenhouse gas emissions. Because Ni-based superalloys are reaching their limits due to their onset melting points of approximately 1300 °C, alternative materials must be interrogated to surpass this ceiling.⁶

Promising alternatives are the refractory complex concentrated alloys^{7,8}. Refractory alloys containing W, Mo, Nb, and Ta are an attractive class of materials for high temperature environments due to their relatively high melting points⁹. However, prior studies of the oxidation resistance and the room temperature ductility of refractory alloys indicate that both properties require significant improvements in order for these materials to be seriously considered as alternatives to Ni-based superalloys.⁸⁻¹⁰

Refractory high entropy alloys (RHEAs) or refractory complex concentrated alloys (RCCAs) are alloys that consist of four or more refractory elements (Ti, Zr, Hf, V, Nb, Ta, Cr, Mo,

and W) in equimolar or near equimolar proportions. The idea behind multiple principal elements is that the configurational entropy (since $\Delta S_{\text{ideal}} = -R \sum_i c_i \log c_i$) of a solid solution can be maximized when elements are in equimolar proportions and increases further when more elements are added.¹¹ A high configurational (or mixing) entropy, in theory, could have a pronounced effect on the phase equilibria, phase transformation kinetics, and lattice distortion, and therefore a pronounced effect on the properties of an HEA or CCA, although some recent work has put the theory of equimolar alloys possessing optimal properties in question.⁹ Nevertheless, this theory resulted in an explosion of research efforts to discover alloys with superior properties than current state-of-the-art alloys and the field has made notable progress with novel alloys in a short time span.^{9,12,13}

There are many notable examples of RCCAs that exhibit high strength at elevated temperatures and possess comparable densities to Ni-based superalloys. The Ashby plot shown Figure 1-1 gives many examples of recently discovered RCCAs with attractive high temperature strength and some with lower densities than Ni-based superalloys.¹⁴ The Ni-based superalloys in the orange region consist of well-known alloys such as Rene 41, Waspaloy, Inconel 718, Hastelloy X, Haynes HR-110, and more. AlNbTiV is an example of an RCCA with comparable strength to these alloys and possesses a lower density. Another notable example is the AlMo_{0.5}NbTa_{0.5}TiZr, which exhibits the highest yield strength from this figure at 1000 °C, and also possesses a lower density than Ni-based superalloys, although further work is required for many of these alloys to assess their room temperature ductility and oxidation resistance.

In terms of progress made in discovering RCCAs that with inherent oxidation resistance by formation of a protective oxide scale, an alloy termed “NV1” was discovered by K.C. Lo *et al.*¹⁵, which is a 7-component alloy containing with a composition of approximately Al17.6-Si2.9-Ti5.4-Cr25.2-Nb15.2-Mo20.3-Ta13.4. Oxidation tests were performed, and the result at 1100 °C for 200 hours and compared to other RCCAs is shown in Figure 1-2. NV1 represents a significant milestone in the oxidation resistance of RCCAs, and it was found that the protective scales formed were CrTaO₄, Al₂O₃, and Cr₂O₃, although it is possible that CrTaO₄ hindered the formation of alumina and chromia. So far, this RCCA possesses the highest oxidation resistance to date when compared to other RCCAs.

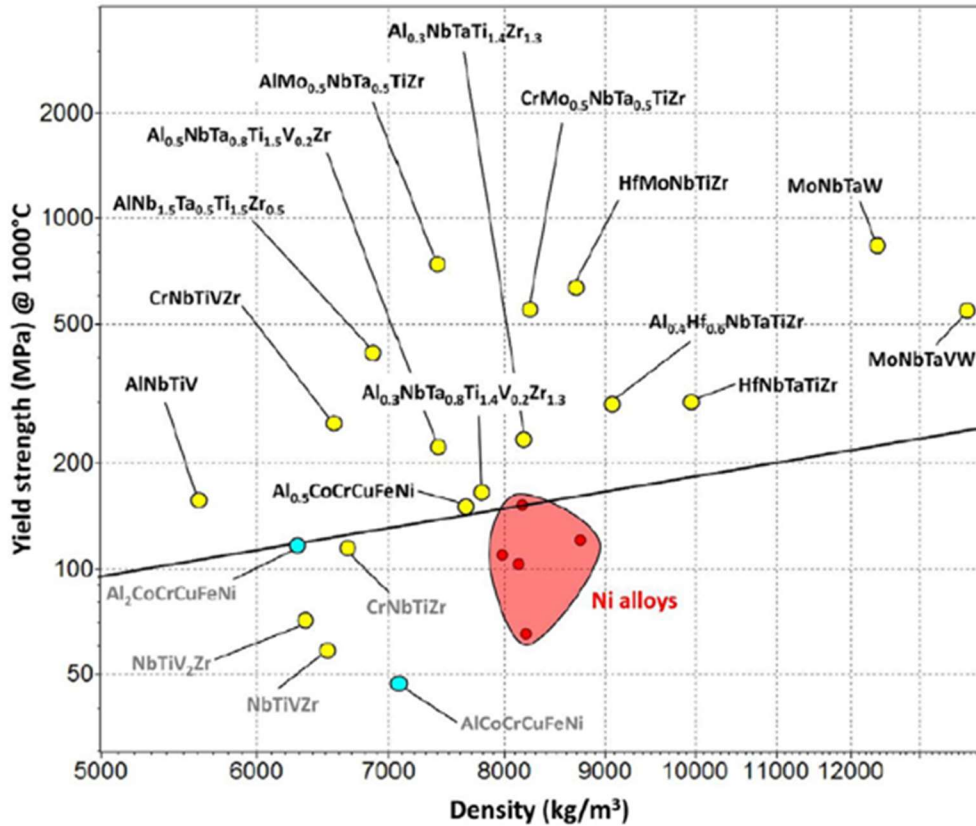


Figure 1-1. Ashby plot showing Ni-based superalloys in the orange region and comparing their high temperature strength to recent works involving RCCAs. Adapted from Ref. [14].

However, there remains a glaring key issue: the vast number of possible alloys to be examined that result when mixing multiple elements in various compositions and concentrations. Serial experimentation alone is not a feasible method of exploration as it is inefficient, wasteful and would require an incredible number of experimental trials. Therefore, exploring the limitless compositional space requires an Integrated Computation Materials Engineering (ICME) approach. ICME, as the name implies, involves integrating computational tools to aid in the identification of novel materials with superior properties.¹⁶ In this approach, the CALPHAD, or CALculation of PHase Diagrams method may be utilized to predict phase fraction, transformation temperature, liquidus and solidus temperatures, aluminum activity, and potentially many more thermodynamic properties.^{9,17,18} Such information is crucial to determining whether an alloy is suitable for a given application. The method requires thermodynamic databases and phase diagrams for multi-component systems, which are gathered from experimental trials. Thermodynamic properties of high order systems (e.g., quaternary and quinary systems), are extrapolated from lower order

systems (e.g., binary and ternary systems). The predictive power of the CALPHAD method has been proven in several previous works of coupling experimental data with the CALPHAD predictions, but there is still much progress to be made concerning the accuracy of these predictions.¹⁹

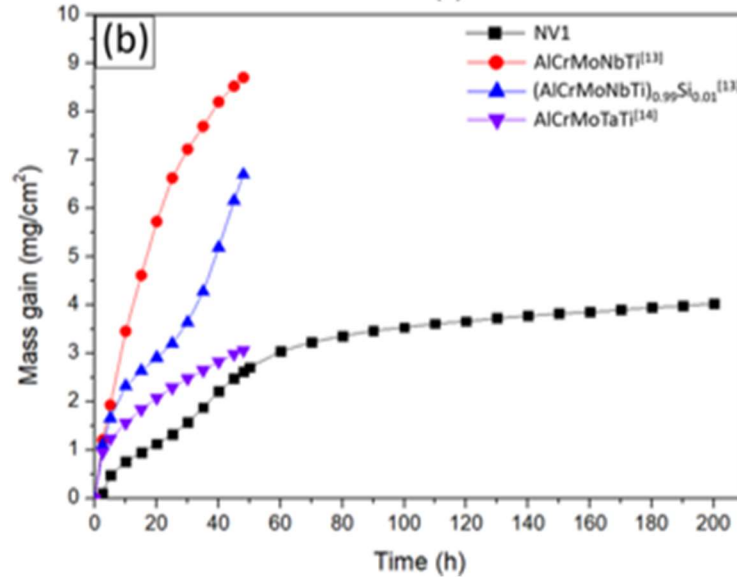


Figure 1-2. Mass gain versus time curve of NV1 at 1100 °C and a total time of 200 hours. This result shows unprecedented oxidation resistance of an RCCA when compared to other RCCAs previously reported. Figure adapted from Ref. [15]. Licensed under CC BY 4.0.

Exploring the compositional space efficiently is also made possible by machine learning, as this method can facilitate discovery and understanding for advanced alloy design efforts.^{20–22} Passive machine learning involves the use of several physics-based descriptors such as mechanical properties, microstructure, and electronic properties to identify trends and facilitate the process of uncovering new materials with attractive properties with limited human interaction.²³ Active learning, on the other hand, is the procedure of selecting a number of candidates for experimental trials based on a balance of exploration and exploitation and a maximum expected improvement in the model and is based on Bayesian optimization frameworks.²⁴ The process can choose to test compositions in an unknown space (exploration), and also choose compositions that theoretically maximize a particular property (exploitation). One such work conducted by C. Wen *et al.*,²¹ exemplifies this approach, and a summary of results is shown in Figure 1-3. The authors employed two different types of active learning approaches: training a machine learning model on the property-composition relationship (termed Loop I), and then introducing physics-based descriptors

related to mechanical properties, such as differences in atomic radii, configurational entropy, valence electron configuration, shear modulus, lattice distortion energy, and many more features (termed Loop II). Through this active learning method, 35 out of 42 alloys exhibited higher hardness than previously reported in literature, with 17 alloys possessing 10% greater hardness than the original training dataset. This work proved the value of utilizing physics-based descriptors coupled with an iterative active learning approach to rapidly discover alloys with high hardness, and that only employing composition versus property based machine learning is not as effective in predicting hardness when implementing features related to mechanical properties in the machine learning model.

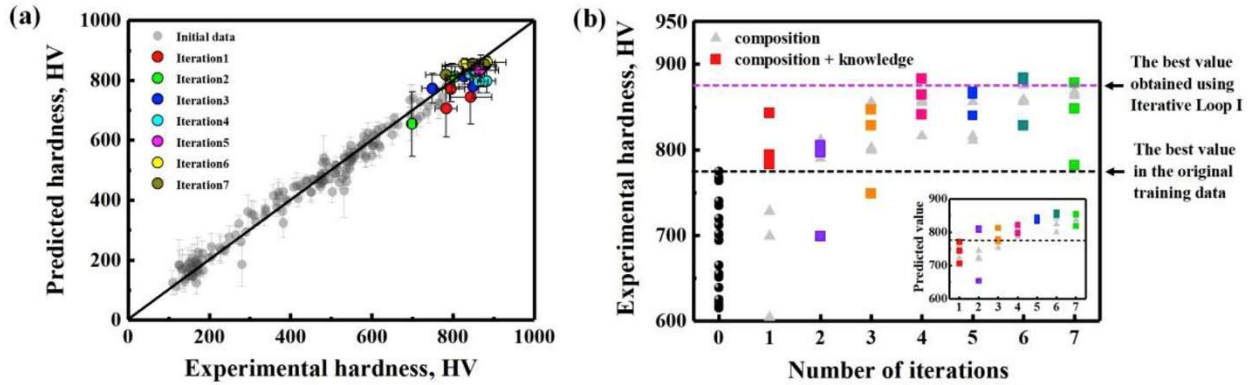


Figure 1-3. a) Hardness parity plot of predicted hardness values and their accuracy when compared to the initial training set. b) Results of active learning loop and differences when using property plus composition (Loop I) versus composition plus knowledge. Adapted from Ref. [21].

For this thesis, a grid of alloys was constructed with justifications provided for the parameters of the grid, and trends with compositions and thermodynamic quantities found by the CALPHAD method (such as Al activity and solidus temperature) were identified. Down-selection and filtering followed this analysis, as the goal of this work was to discover alloys with certain properties, such as a single-phase microstructure, high solidus, and high hardness. A second design objective is to select possible alumina formers by incorporating Al and maximizing activity of Al. Figure 1-3 shows the main goals previously mentioned; the specific strength of some RCCAs surpass that of Ni-based superalloys, but the oxidation resistance still needs improvement, and a comparable mass gain to Ni-based superalloys with higher specific strength is ultimately the goal of this work (e.g., mass gain of 1 mg/cm² and specific strength of 70 MPa cm³/g). Once the final

subset of alloys was selected, an active learning loop was employed for rapid exploration and exploitation of the RCCA compositional design space of single-phase alloys.

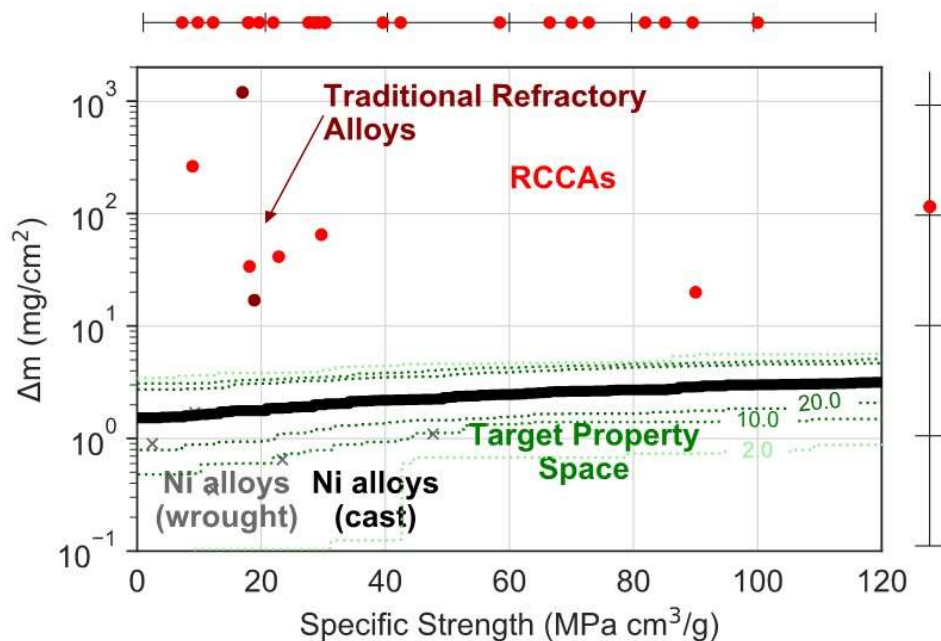


Figure 1-4. A plot showing the mass gain over area versus a specific strength. Ni-based superalloys currently provide superior oxidation resistance than any RCCA, but there are some RCCAs with a higher specific strength. The target property space is a specific strength of 70 MPa cm³/g and a mass gain of 1 mg/cm².

2. A CALPHAD-BASED APPROACH TO DESIGN REFRACTORY CONCENTRATED COMPLEX ALLOYS CAPABLE OF FORMING A CONTINUOUS Al_2O_3 PROTECTIVE SCALE UPON OXIDATION AT 1000 °C

2.1 Introduction

The CALPHAD method utilizes the principle of the Gibbs energy minimization at a given temperature and pressure to predict the equilibrium state of a system. The thermodynamic description is stored in a database, which is then used by software such as PANDAT and Thermo-Calc to construct phase diagrams.¹⁶ For multi-principal element alloys (MPEAs), the thermodynamic descriptions of lower order systems such as binaries and ternaries are extrapolated to construct a higher order thermodynamic database. The downside of the method comes in the attempt to derive phase diagrams of multi-component systems, where there is simply not enough data to make a truly accurate prediction on the equilibrium phases of a CCA. Numerous experimental works have verified the accuracy of CALPHAD predictions for some systems (depending on the composition of the alloy), such as the work of Manzoni *et al.*²⁵ Manzoni evaluated the AlCoCrCuFeNi system which includes brittle alloys with intermetallic phases, by making several adjustments to the composition and studying the effects of heat treatments at various conditions and comparing the observed phases to phases predicted by Thermo-Calc, which showed agreement on some alloys.

The goal of this work is to explore the compositional space of RCCAs and determine possible $\alpha\text{-Al}_2\text{O}_3$ scale forming alloys. The CALPHAD method has been employed along with a high-throughput approach. High-throughput methods and experimentation have been utilized heavily in the pharmaceutical industry to rapidly discover novel drug compounds and, as a result, has greatly accelerated drug research and development²⁶. The same process of screening can be applied to computational approaches for advanced alloys. High-throughput screening using the CALPHAD method is ideally capable of accelerating the goal of discovering high strength, oxidation resistant alloys by computing the stability range of the BCC phase, aluminum activity, and melting onset temperatures across hundreds of alloy systems. Further acceleration of alloy discovery can be facilitated using machine learning models and an active learning loop^{27,28}, which will be elucidated in the following chapter of this thesis.

2.2 Construction of Initial Compositional Design Space

To begin the high-throughput screening process, a palette of elements, a step size between compositions, and the number of elements for any given system must be defined, and the palette of elements is shown in Figure 2-1⁹. In this work, alloys with the nine refractory elements mentioned previously, in addition of aluminum for oxidation resistance, with a 5 at% step size, were used to construct the grid of alloys for the computation of thermodynamic properties for all possible combinations of four component, Al-bearing RCCAs. A 5% step size was chosen for this dataset for a reduction in computational time, to expedite the active learning process, and to mitigate the possibility of testing alloys close in composition. To further expedite the calculations, alloys containing greater than 40 at% aluminum were disregarded as intermetallic formation with high a percentage of aluminum was of great concern, and a large drop in solidus temperature was also expected.

The thermodynamic quantities calculated were equilibrium phases, volume fraction of phases, activity of Al, solidus and liquidus temperatures, densities, BCC solvus temperatures, and the crystal structure of each phase (only differentiating between intermetallic and BCC solid solution phases). After the thermodynamic properties of the initial design space were computed, further filtering was required for selection of alloys exhibiting single phase BCC microstructures (i.e. a volume fraction of solid solution BCC equal to unity) at 1000 °C, and for feasibility of fabrication through solidification processing. Several scripts were written in the programming language Python, using the SDK TC-Python and the thermodynamic database for high entropy alloys, TCHEA4.

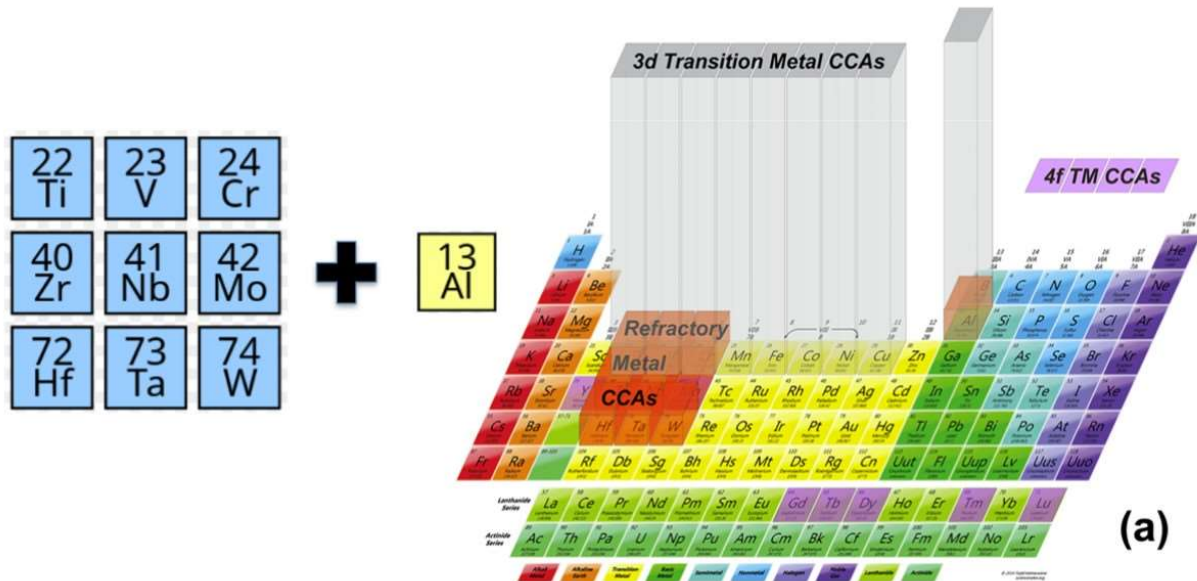


Figure 2-1 The elemental palette considered. It consisted of the 9 refractory elements (Ti, Zr, Hf, V, Nb, Ta, Cr, Mo, and W) plus Al for oxidation resistance. Adapted from Ref. [9]. Licensed under CC BY 4.0.

2.3 Computational Methods: Scripts Created for the Down-Selection of a Grid of Alloys

2.3.1 Get_phases_and_structures

The `get_phases_and_structures`²⁹ function allows for a quick and easy assessment of the equilibrium phases present in any given alloy and the volume fraction of these phases. The composition and temperature of an alloy were inputted, and the equilibrium phases and their volume percentages at that temperature were found using the `get_stable_phases` function in the `tc_python_plotter` python file.

The sublattices of the equilibrium phases were evaluated using the `calc_sublattice` function, which provided dictionaries of the site fractions of an element in a phase. The contents of the dictionary were then evaluated. If the keys (keys are the subject that a value is assigned to, e.g., if the element Al has an atomic fraction of 0.4, then the key value pair is “Al: 0.4”) of the value and values of the first two dictionaries outputted were equal, then this phase was considered disordered. The phase was then assigned to have a value of ‘SS’, which meant that the phase was a solid solution. Otherwise, if the outputted dictionaries were found to be different, then the phase was assigned as ‘IM’ meaning an intermetallic or ordered phase.

A dictionary was created of all phases and their assignments, and an overall assignment for the alloy was generated; if only SS phases were present in the alloy, then the alloy was assigned as ‘SS’. If there were both SS and IM phases present, then the alloy was assigned as ‘SS+IM’. If there were only intermetallic phases present, then the alloy was assigned as ‘IM’.

Furthermore, a one-hot encoding term was created based on the phases present and the assignment generated for the alloy. If only FCC and BCC solid solution phases (i.e., phases assigned ‘SS’) were present, then the encoding term was ‘FCC+BCC’. If the previous condition was true, but there were intermetallic phases present, then the encoding term was ‘FCC+BCC+Secondary’. If there were solid solution BCC or FCC phases and intermetallic phases present, then the encoding term was ‘BCC/FCC+Secondary’. If the alloy consisted of a single FCC/BCC phase, then the encoding term was ‘FCC/BCC only’. Otherwise, if an alloy only contained intermetallic phases, then the encoding term was ‘Other’.

This function provided, in a dictionary, the stable phases present in an alloy at a given temperature, the crystal structure of those phases, the general crystal structure of the alloy, the volume fraction of all phases, and the one-hot encoding term for the alloy. This information was then used to filter out alloys based on a number of criteria, such as single phase only, volume fraction of BCC phase, and so on.

2.3.2 Try_calculating_solvus

The `try_calculating_solvus` function was built due to internal issues from ThermoCalc that arose from calculating the solvus temperature of the BCC phase for certain alloys. It utilized the `calc_transformation` function of the `tc_python_plotter` package, which required several parameters: the phase of interest, the volume fraction of that phase, and the reference temperature, which needed to be close to the theoretical solvus temperature of the phase of interest.

The function was used to identify the stable phases in the alloy, to check if the BCC phase was present, and to check if the solidus temperature was calculated; this was necessary because the `calc_transformation` function sometimes returned a temperature that was equal to the solidus temperature, even if the reference temperature was over 50% different from the solidus temperature. In which case, the `try_calculating_solvus` function scanned a range of temperatures in 50 K increments starting at 150 K and ending at 2500 K. The starting points and

ending points were chosen after evaluating the accuracy of Thermo-Calc's predictions at the extremes of temperature.

The function was then used to evaluate, at each incremental temperature, if the solvus was calculable. If an error was returned after attempting to calculate the solvus temperature, or if the solvus temperature returned was equal to the solidus temperature, then the function continued to scan through the range of temperatures until a value not equal to the solidus temperature was returned, or the 2500 K limit was reached. If the limit was reached and no solvus temperature was found, then the solvus returned was simply "None".

2.3.3 Get_fabrication_method

In earlier experimental trials to fabricate an alloy of CrMoW through arc melting, it was found that there was significant loss of Cr and extremely large void formation that likely resulted from evaporation of Cr. The Cr boiling point is approximately 2672 °C³⁰, and the binary equiatomic alloy of MoW has a liquidus temperature of approximately 3200 °C³¹. Clearly, the incorporation of Cr in liquid MoW, or even just pure liquid Mo and liquid W can cause significant mass loss of Cr. Furthermore, Al has a boiling point of approximately 2470 °C³² and it can be inferred that a similar attempt to incorporate Al into an equiatomic MoW alloy could result in significant mass loss through evaporation. Figure 2-2 shows the differences in boiling and melting points of Al and Cr and the melting points of other refractory elements.

A workflow was developed to split the alloy processing into two different methods - arc melting or powder metallurgy. The workflow functioned as follows:

1. Calculation of the liquidus temperature with nominal amounts of Cr and/or Al.
2. Calculation of the liquidus temperature of the alloy upon removing Cr and/or Al.
3. If the liquidus of the Al-bearing alloy, or the liquidus of the Al- and Cr-free alloy exceeded the boiling point of Al, then the powder metallurgy route was the recommended process.
4. If the liquidus of the Al- and Cr-free alloy was less than the boiling point of Al, then arc melting was the recommended process.

This function was written as an attempt to mitigate Al and Cr loss by filtering out alloys that contained high melting point elements such as Nb, Ta, Mo, and W and that would likely evaporate

large amounts of Al and Cr if fabrication was conducted by arc melting. The powder processing route was a more viable option for the fabrication of alloys with high melting points, as processing steps such as the Pechini method and mechanical alloying do not involve the metal alloy liquid state or temperatures exceeding the boiling points of Al and Cr.

A function that can be utilized to generate homogenization windows of compositions was also formulated but was not used in the work as expediting the active learning process was of the highest priority. This function is included in the appendix.

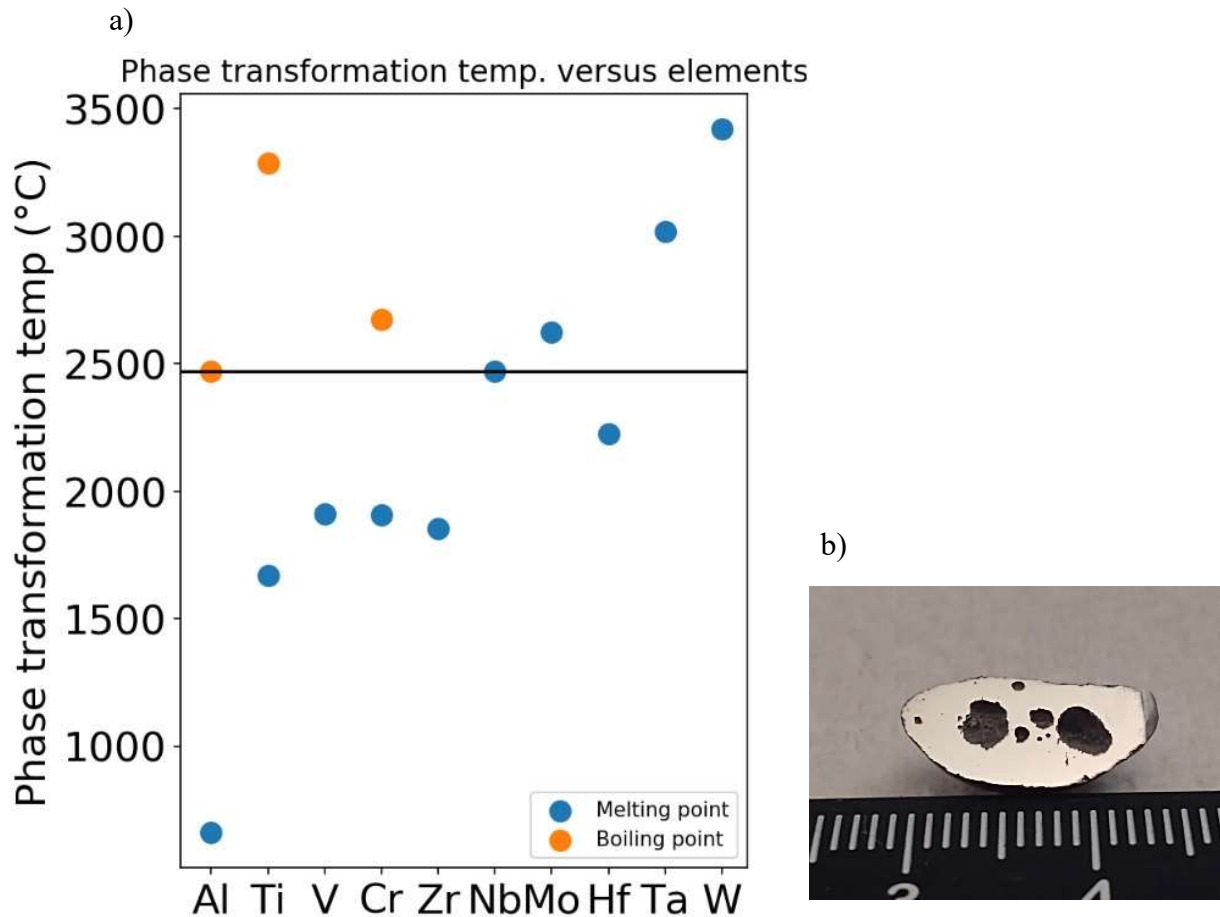
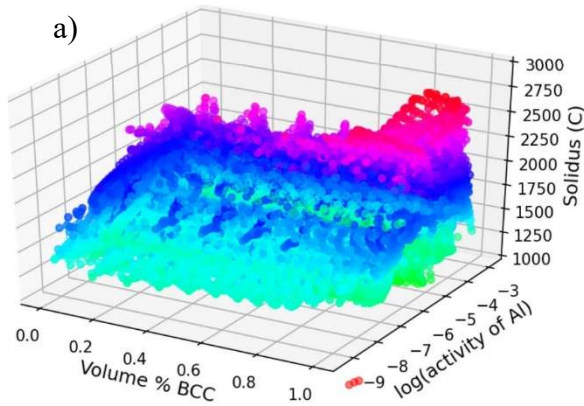


Figure 2-2 a) A graphical representation of the boiling point issue when melting volatile elements such as Al and Cr with high melting point elements such as Mo and W. The `get_fabrication_method` function aimed to solve this issue. b) An attempt at arc melting a CrMoW alloy that underwent significant Cr vaporization and formation of large pores.

2.4 Results and Discussion

Visualization of the data is key to discovering trends in thermodynamic properties with composition. A 3D color map of the unfiltered design space at 1000 °C is shown in Figure 2-3a, where the red and pink dots indicate compositions with relatively high solidus temperatures. Their location also reveals aggregations near the single-phase region, as well as high Al activity, which suggested compositions with higher melting point refractory elements, such as W and Mo, and potentially high Al contents with high volume fractions of the BCC phase. In Figure 2-3b, the ideal mixing entropy is plotted as a function of composition over all alloy systems. While such a plot could yield alloys with a “high entropy” effect that is said to stabilize the single phase region^{33,34}, there was little variation in the color over the entire plot; that is, alloys with particularly high entropies were not clearly identified from this plot.

Mapping of 67,440 4-Component Al Containing Alloys



t-SNE Plot for visualization of composition data

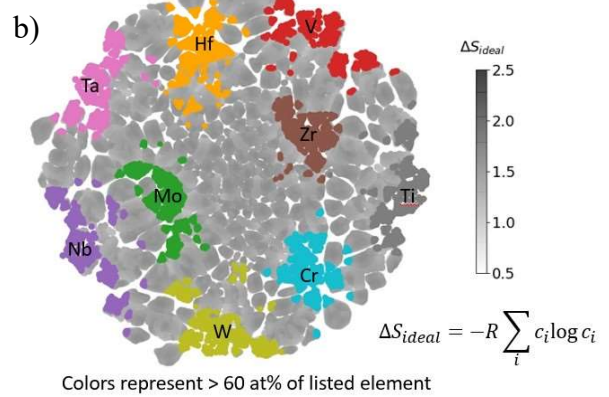


Figure 2-3 . a) 3D color mapping of the initial design space. b)t-SNE plot with ideal mixing entropy plotted with a greyscale.

The filtering steps were then applied; that is, the scripts mentioned in the previous section were used to filter out alloys that were not single-phase BCC, and to filter out alloys with a BCC solvus temperature higher than 1000 °C. This reduced the design space dramatically from 67,440 compositions to 6,522 single phase compositions. Another t-SNE plot has been provided in Figure 2-4, revealing large gaps in the compositional space. It was evident that the single-phase compositions tended to aggregate around a base element, especially in the case of W, Ta, and Hf. The single-phase alloys were then separated by the `get_fabrication_method` function into

two categories depending on fabrication method: arc melting or powder processing. There were 5,144 alloys deemed “arc-melttable” and 1,378 alloys suggested for powder processing, both of which are shown in Figure 2-4, with the black dots indicating the alloys present after applying the filter methods.

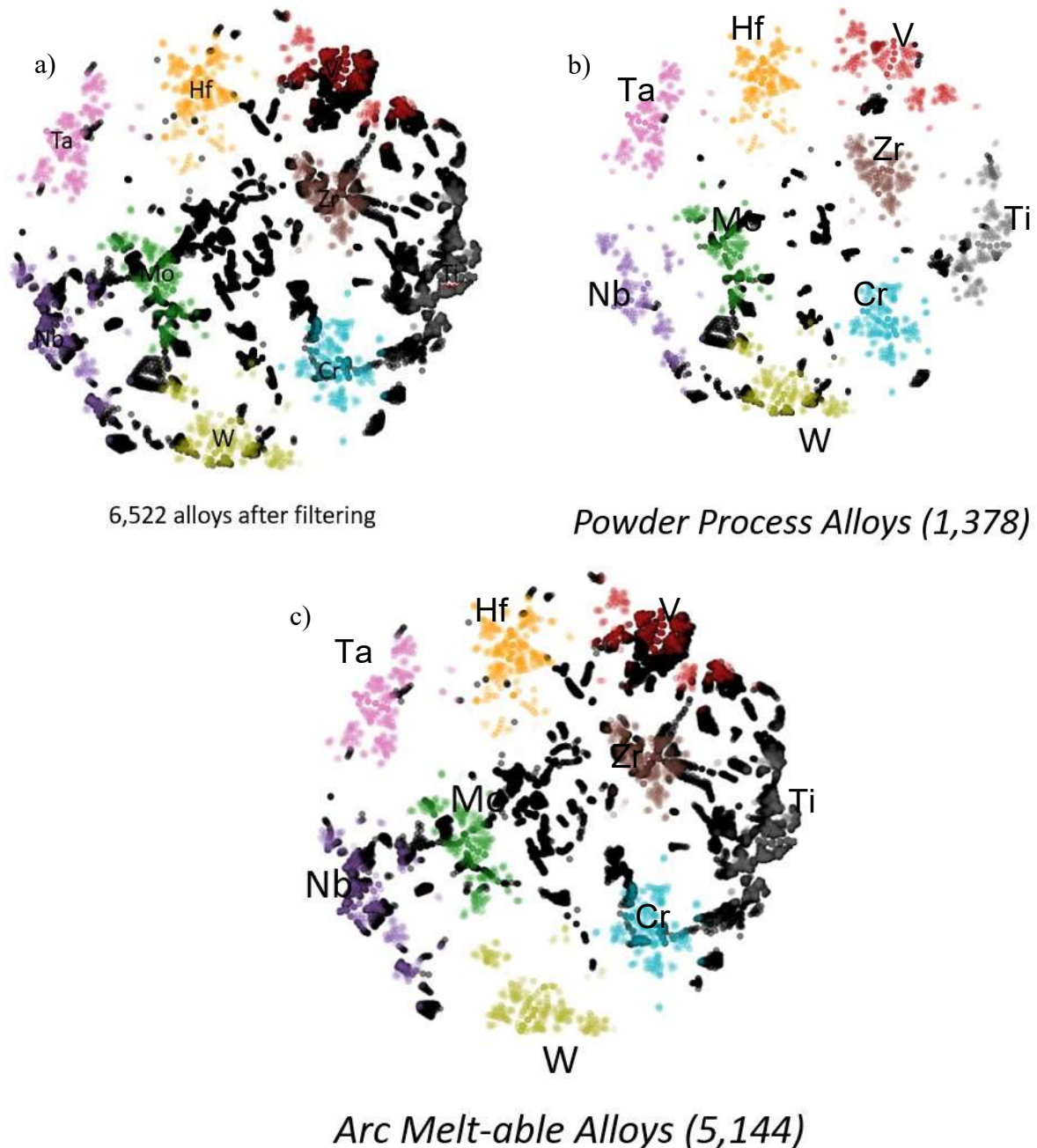


Figure 2-4 a) All alloys that are single phase and possess a BCC solvus temperature lower than 1000 °C. b) Powder processing alloys. c) Arc melttable alloys.

The frequency of an element occurring in both fabrication design spaces can be quantified as well (Figure 2-5). Unsurprisingly, the number of single phase BCC compositions containing Zr were low, as Zr forms more intermetallic compounds with Al than compared to other elements.³⁵ There were also few Hf containing compositions, as Hf has similar bonding characteristics as Zr with respect to Al.³⁶ It was also apparent that there were a high number of Ti-, V-, Nb-, and Mo-containing compositions in the arc melting category, and relatively high numbers of V-, Nb, and Mo-containing compositions in the powder metallurgy space. However, the number of Ti-containing alloys dropped off dramatically for powder metallurgy processed alloys. In both categories, there were relatively few compositions for Cr and Ta, but these elements also form a high number of intermetallic compounds with Al.^{17,37}

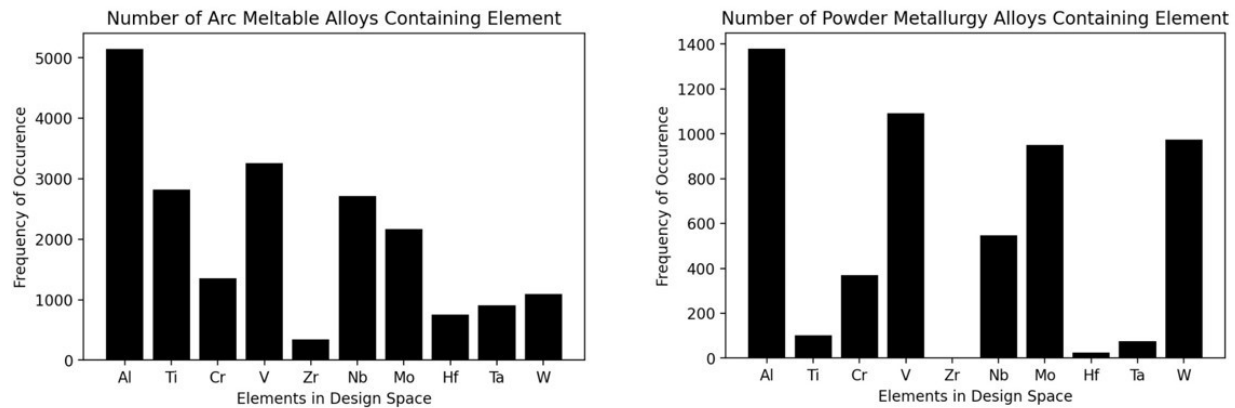


Figure 2-5 The frequency of elements in the compositions of both fabrication methods. Elements with some solubility at high temperature with Al (V, Nb, Mo, Ti) show a good number of single phase compositions, and those that readily form intermetallic compounds (Cr, Zr, Hf, and Ta) are low in quantity.

Investigating the Pareto front of the Al activity and solidus temperature can also provide insight into the types of systems and compositions that are the most optimized in terms of those quantities (the compositions that simultaneously maximize the Al activity and the solidus temperature). Al activity can possibly be used as a surrogate for oxidation resistant alloys, although it is only one factor in terms of forming a protective alumina layer.⁴ Nevertheless, it provides a starting point and can allow an efficient means of testing compositions sequentially. The Pareto front between the solidus temperature and Al activity for both processing methods are shown in

Figure 2-6a, b, and the systems and frequency of the systems along the front are given as well in 2-6c, d.

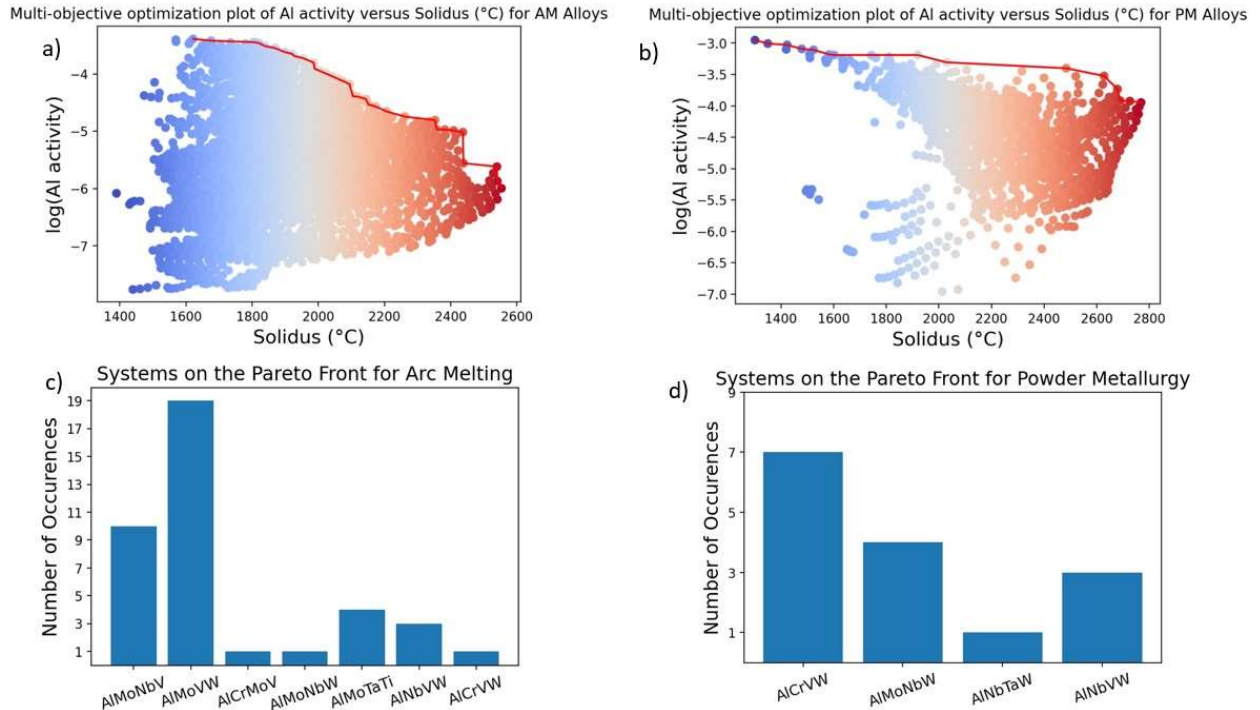


Figure 2-6 a) Multi-objective optimization plot and Pareto front for arc melt-able alloys. b) Multi-objective optimization plot and Pareto front for powder processing alloys. c) Quantity of systems that lie on the Pareto front of arc melt-able alloys. d) Quantity of systems that lie on the Pareto front of powder processing alloys.

40 and 15 compositions lie on the Pareto front for AM and PM methods, respectively. The Al compositions for both fabrication methods ranged from 0.05 to 40 at%, and Al activity for the AM method ranged from 1×10^{-6} to 0.000408 whilst Al activity for PM methods ranged from .000113 to .00112, which is remarkable as a drop in at% of Al from 40 to 5% was associated with a only drop of a single order of magnitude in Al activity. A summary of the minimum and maximum activity and solidus temperature as well its composition is provided by Table 2-1.

Table 2-1 Comparison of compositions with minimum and maximum optimized values.

Composition (at%)	Al activity	Solidus (°C)	Fabrication method
Al5.0Mo40.0Ta30.0Ti25.0	1e-6 (min)	2553 (max)	Arc melt
Al40.0V30.0W15.0Cr15.0	.000408 (max)	1621 (min)	Arc melt
Al5.0Mo30.0Nb5.0W60.0	.000113 (min)	2768 (max)	Powder
Al40.0V10.0W45.0Cr5.0	.00112 (max)	1301 (min)	Powder

Hardness predictions were computed for all single-phase BCC compositions, and a correlation heatmap was created for both fabrication subsets, with the hardness predictions, at% of elements, and thermodynamic quantities plotted against each other to observe correlations between predicted hardness and the mentioned quantities. The correlation heatmap for arc melt-able alloys is shown in Figure 2-7, and the heatmap for powder processing alloys is shown in Figure 2-8.

The correlation plot for arc meltable compositions show some trends in the predicted hardness (left-most column in Figure 2-7), namely that at% Al, has a strong positive correlation with Al activity, at% W has a weak positive correlation with Al activity while at% Ti, enthalpy of mixing of the system, and mixing entropy and the solidus temperature have negative medium correlations with Al activity. Enthalpy of mixing has a strong negative correlation with at% Al, and medium positive correlation with at% Hf, Ta, Ti, and mixing entropy. Entropy of mixing has medium positive correlations with at% Hf, Zr, Ta, and Ta and medium negative correlations with at% Al, V, W, Cr, and Al activity. Correlations for the PM compositions exhibited similar relationships when compared the AM compositions.

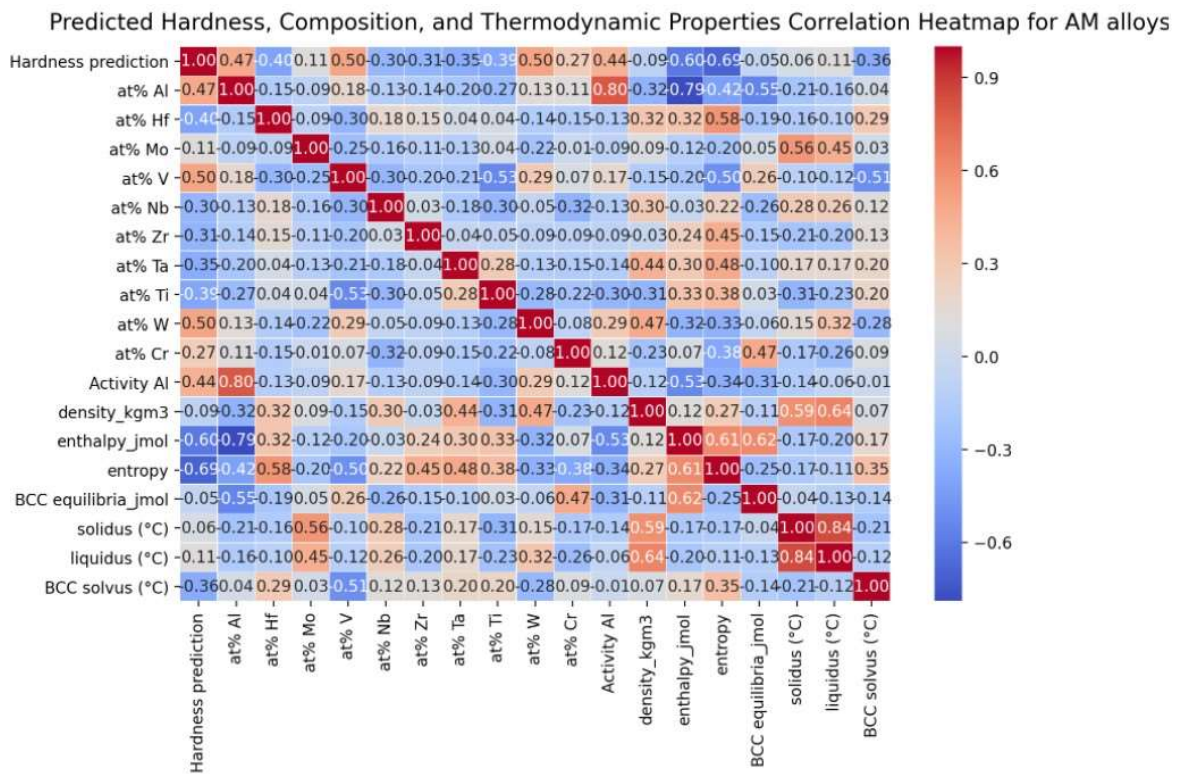


Figure 2-7 Correlation heatmap between the predicted hardness of all single-phase arc melttable alloys.

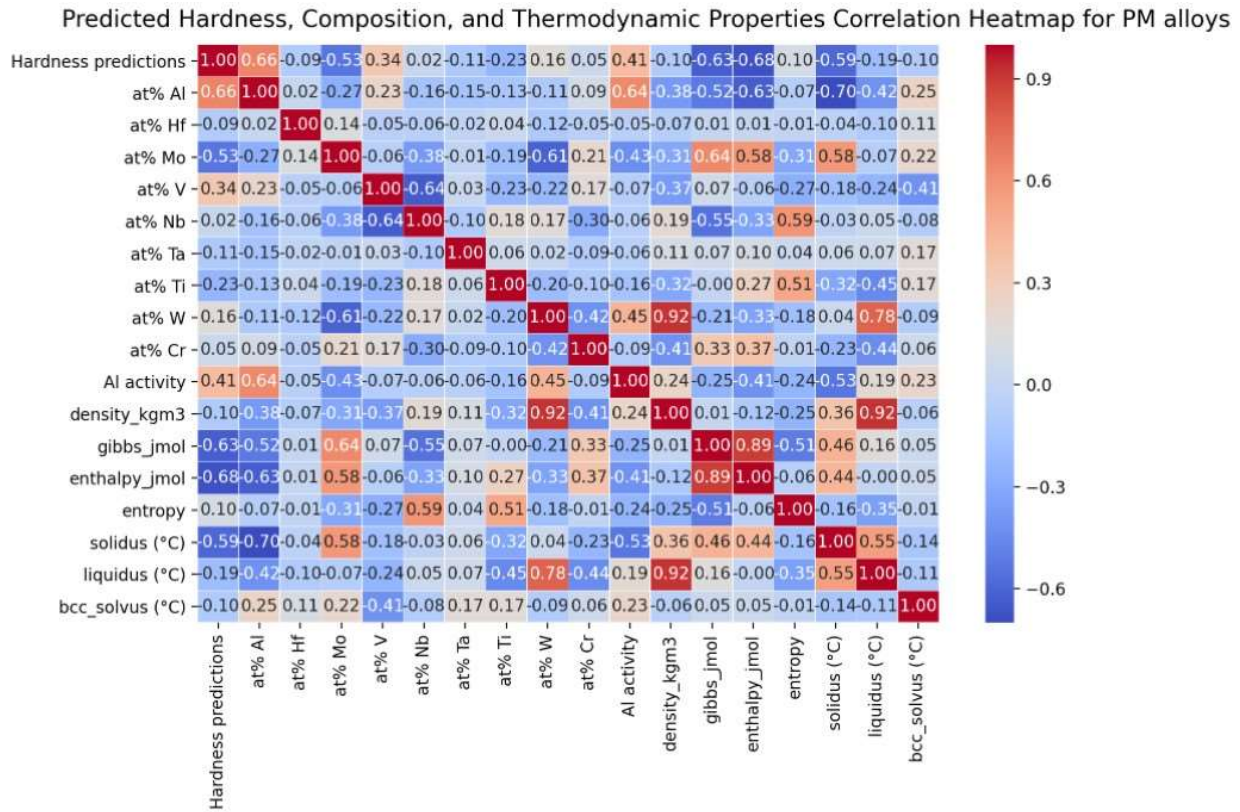


Figure 2-8 Correlation heatmap between the predicted hardness of all single-phase powder processing alloys

2.5 Conclusions

In summary, a set of conditions were placed upon a grid of alloys, and the thermodynamic quantities pertinent to high strength, high oxidation resistant alloys such as solidus temperature, activity of aluminum, and presence of a solid solution phase were calculated at 1000 °C. With restraints such as 4 components, a 5% step size, a maximum Al percentage, and the 9 refractory elements, thermodynamic properties were calculated in a rapid fashion, and then further down-selected to a smaller, more manageable subset with the goal of performing high-throughput experimental trials for further alloy discovery. By using scripts that take into account the processability of any given composition, it was possible to parse out the subset further and recommend certain fabrication methods. This technique resulted in compositions that were recommended for powder processing to be high in high-melting point elements such as Mo and W, as attempting to make alloys high in these elements by solidification processing would likely cause significant evaporation and mass loss.

Through the use of a suite of data visualization tools, trends were elucidated, and key areas of the design space worth further exploration were identified. Essentially, it was found that there was a concentration of V-based alloys in both processing methods, likely due to the large solubility of Al in V at high temperatures³⁸, whereas other elements such as Zr, Hf, Cr, and Ta show little Al solubility in the binary phase diagrams.^{17,35–37} Promising alloy systems on the Pareto front optimizing Al activity and solidus temperatures were identified for future work for testing such alloys. Correlation heatmaps yielded trends relevant for alloy design, such as the W content in relation to Al activity and predicted hardness versus atomic percent of certain elements.

3. HIGH-THROUGHPUT EXPERIMENTATION FOR THE DISCOVERY OF HIGH STRENGTH ALLOYS BY ACTIVE LEARNING

3.1 Introduction

As there were a large number of possible RCCA compositions to evaluate, a strategy was needed to efficiently examine the design space based on a target property. Machine learning has been proving to be an extremely effective tool for reducing the time and effort required to discover new drugs²⁶, track business trends³⁹, evaluate biological impacts of changing ecosystems and climate⁴⁰, assess legal works, identify efficient methods of transportation⁴¹, and other applications to benefit society.

The field of materials science has also seen significant benefit from use of machine learning to analyze large amounts of materials data, either compiled neatly in an easily accessible format, or manually searched for in the literature. Researchers have been able to identify trends in material properties based upon several different inputs such as atomistic (e.g., valence electron configuration (VEC), average atomic radius, and atomic volume misfit), mechanical properties, and thermodynamic information (ab initio simulations and CALPHAD predictions).^{21,22,41} However, there is still a need for experimental trials to accelerate materials discovery and confirm materials properties. A machine learning accelerated materials discovery framework with a clear set of goals is necessary for undertaking this task. A set of low- and high-fidelity experiments, and a schematic of the framework used in this work is shown in Figure 3-1. In this work, the low-fidelity, high-throughput experiments were given priority and high-fidelity, “low throughput” experiments reserved for future work (once a set of alloys with desirable properties have been discovered with low-fidelity experimental trials).

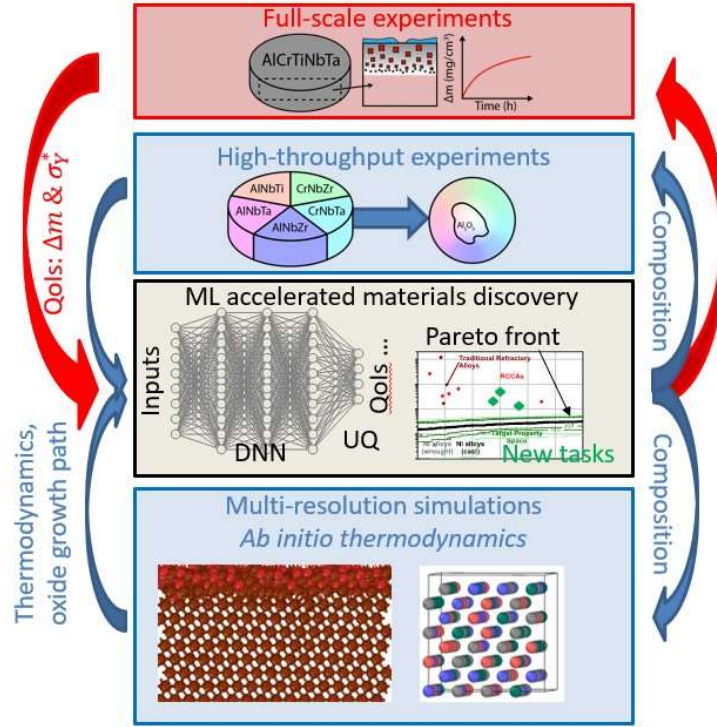


Figure 3-1 The proposed machine learning accelerated materials discovery framework that combines machine learning, ab initio simulations, high-throughput (low-fidelity) and full-scale (high-fidelity) experiments. Target metrics are a low mass gain in oxidizing environments and high strength. From NSF DMREF proposal

To combine machine learning and design of experiments (DOE), an active learning procedure was utilized. Active learning is the process of using machine learning models to predict the properties from an array of possible experiments in a design space containing unknown properties in order to fill in the gaps of uncertainty with targeted experiments.^{21,27} A set of experiments is then chosen based on either the maximum expected improvement of a property (Vickers hardness in this study), or the maximum uncertainty of an area in the design space. The batch of alloys are then characterized, the data gathered is used to amend the model, and a new batch of experiments is suggested. An illustration has been provided in Figure 3-2.²⁷ This procedure, termed an active learning loop, is repeated until the expected improvement has reached a maximum and multiple alloys with desirable properties are found.

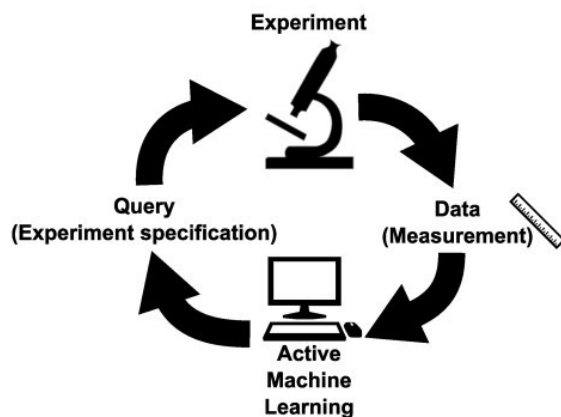


Figure 3-2 A simplistic schematic of the active learning procedure, and a similar process is followed in the present work. Adapted from Ref. [25]. Licensed under CC BY 4.0.

In this work, the active learning loop was focused on maximizing Vickers hardness (HV), as the HV and yield strength exhibit good correlations in steels, bronzes, Al alloys, Ni-based superalloys, and other alloy families⁴². A review of the present HEA database published by Cristopher Borg *et al.* in 2020⁴³, reveals that, for all microstructures (BCC, FCC, and multi-phase), the hardness shows good correlation with the yield strength (Figure 3-3b), so that hardness may be used as a surrogate characteristic for strength.⁴² Another possible surrogate model for strength is grain size, as it well-known that the Hall-Petch relationship can be used to predict strength, but upon analyzing the data (Figure 3-3a), there is a large variation in strength depending on the processing method. Further analysis of the database, shown in Figure 3-4, reveals that there is a stunning lack of data on the hardness of single phase, 4-component, Al-bearing alloys with the 9 refractory elements (only 3 entried), which is the design space of this study. The absence of data also implies that there is largely unexplored compositional space in this sector of HEAs, and this work was aimed at filling a substantial gap in knowledge. The three aforementioned alloys are equimolar compositions of AlMoNbTi (HV: 509, As-Casted), AlNbTaTi (HV: 458, As-Casted), and AlNbTiV (HV: 448, annealed). Discovering RCCAs that surpass the hardness values of these three reported alloys is a key goal of this study.

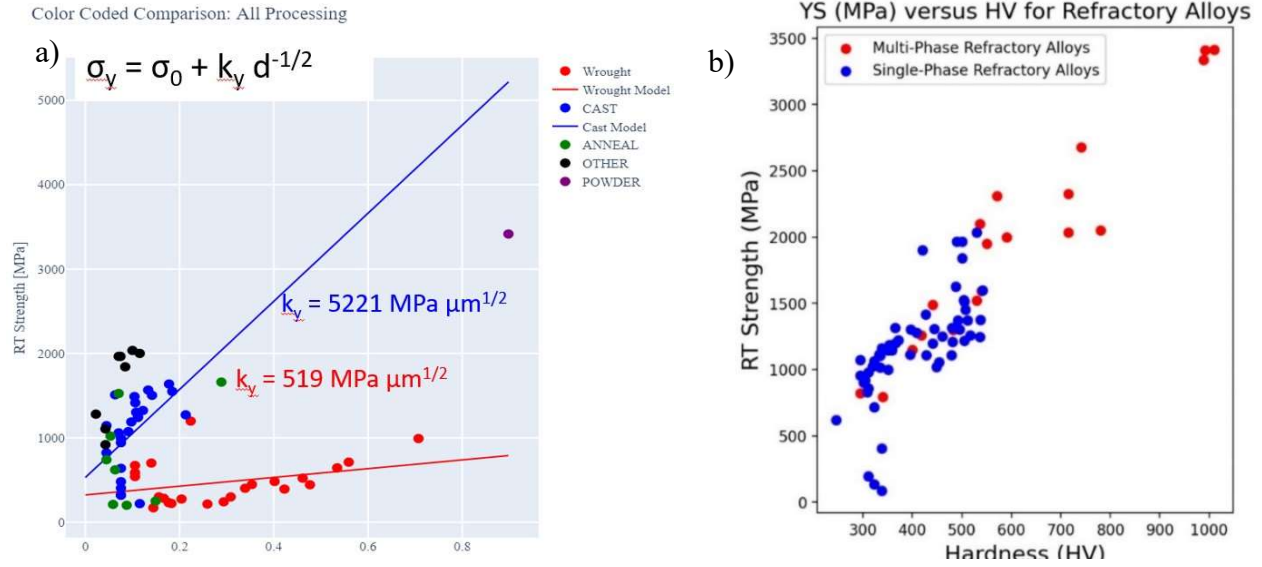


Figure 3-3. a) A comparison between RT yield strength and grain size of different processing methods. b) An analysis of the Vickers hardness and room temperature strength of both multi- and single-phase alloys from the HEA dataset.

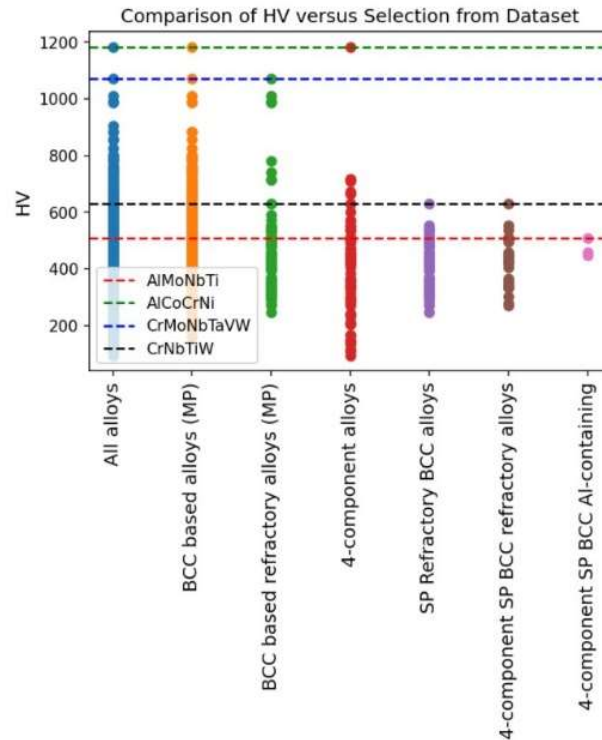


Figure 3-4. Visualization of the number of alloys with hardness data that belong in each design space. By reducing the dimensionality of the design space, it is revealed that there is a large gap in knowledge of strength for single phase, Al-bearing, 4-component RCCAs.

3.2 Methods

3.2.1 Method of Alloy Selection: Active Learning Using Bayesian Global Optimization

Sharmila Karumuri is credited for this work. Bayesian global optimization (BGO) deals with solving the problem shown below with limited budget evaluation:

$$x^* = \operatorname{argmax} E(y|x) \quad (3-1)$$

where x^* is the location of the next experiment, $\operatorname{argmax} E$ is the acquisition function, y is the input hardness, and x are the input descriptors used to predict hardness (melting point, volume atomic misfit, average atomic radius, asymmetry of atomic radii, reduced phase one-hot-encoding, VEC, entropy of mixing, density, solidus and liquid temperatures, range of Young's modulus, range of density, range of melting points, range of bulk modulus, range of VEC, and range of atomic radii). BGO involves optimization by sequential information acquisition and is an algorithm that determines the next experiment based on interested in minimizing/maximizing a value. The location of the next experiment is then found by maximizing a function called the acquisition function (AF) at $a(x)$, where $a(x)$ is expected improvement. The AF quantifies how much information there is in evaluating at x , which is the next experiment.

There are multiple steps in conducting such a process, and a flowchart is shown in Figure 3-5:

1. Start with an initial dataset.
2. Construct a surrogate model using Gaussian process.
3. If enough computational/experimental budget is available, proceed to the next step and the next experimental location is chosen.
4. Select the next experiment location at x' based on where the AF determines there is a maximum expected improvement (EI)
5. Perform experiment at x' and get the quantity of interest y'
6. Add new data and repeat from step 2

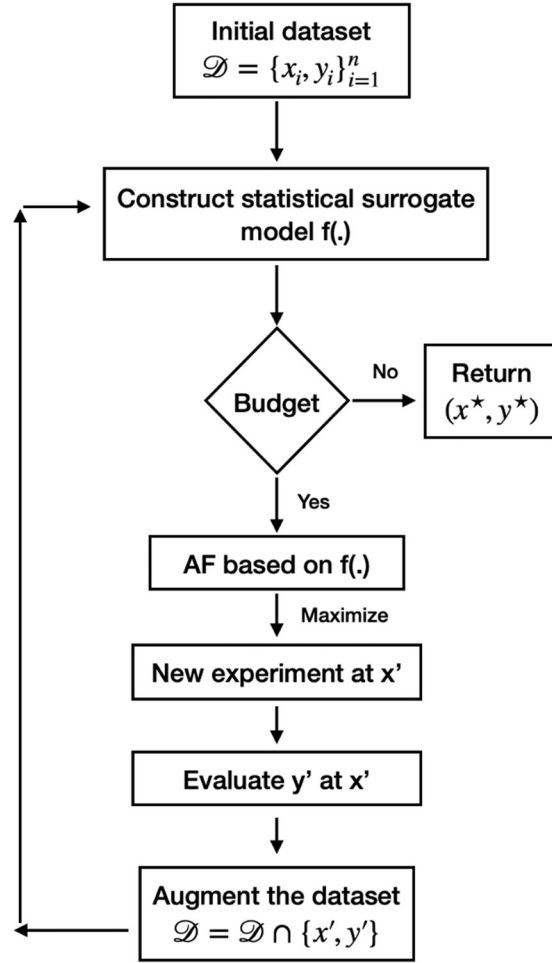


Figure 3-5. A flow chart summarizing the Bayesian Global Optimization process. This figure is credited to Sharmila Karumuri and Ilias Bilionis.

For the purpose of this study, the process has been amended and a batch of ‘m’ compositions is recommended for testing. The EI is used as our AF $a(x)$, which will both explore and exploit the design space:

$$a(x) = EI(x) = (m(x) - m^*) \Phi \left(\frac{m(x) - m^*}{\sigma(x)} \right) + \sigma(x) \phi \left(\frac{m(x) - m^*}{\sigma(x)} \right) \quad (3-2)$$

where $m(x)$ is the predicted mean hardness of alloy x , $\sigma(x)$ is the uncertainty of hardness of alloy x , m^* is the maximum hardness in dataset, Φ and ϕ are cumulative and probability density functions, respectively, chosen to exploit and explore the design space. In the original BGO process, the algorithm suggested a single experimental location for each iteration. Clearly, a single experiment per iteration would be insufficient in a high-throughput effort to discover RCCAs with optimal

properties, so a batch of ‘m’ compositions was suggested instead. However, the previous algorithm would suggest alloys close in composition at the top ‘m’ max location of the AF, so the process needed to be amended to overcome this issue as shown in Figure 3-6.

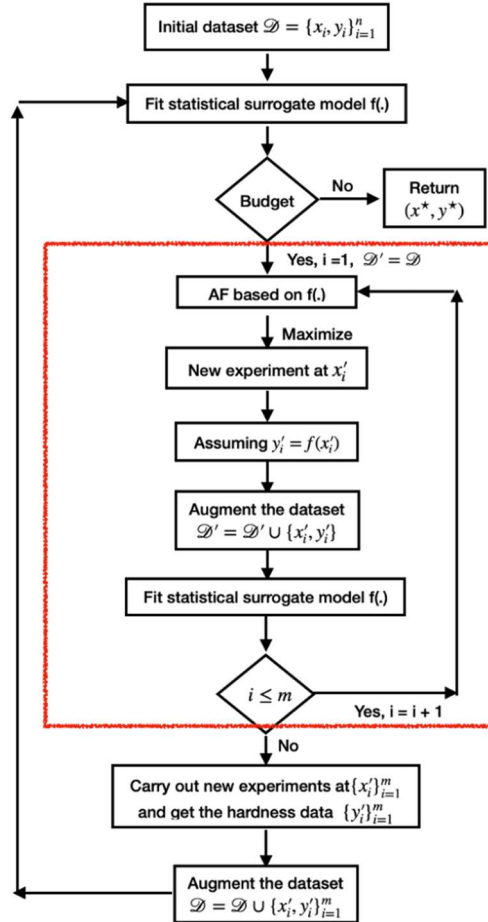


Figure 3-6. The amended BGO process showing the primary differences from a regular BGO process. The model assumed the experimental data was equal to the predicted hardness, which was then fed back into itself to compute a new maximum EI value for identifying the next alloys. This figure is credited to Sharmila Karumuri and Ilias Bilonis.

The amended algorithm was similar to the general BGO process, but the inner loop was changed (highlighted in the orange box in the figure) so that the top ‘m’ experiments were diverse in composition. For the first experiment suggested in a batch, the usual BGO procedure was followed where the AF was maximized. The change in the process came in the second alloy suggested; the algorithm assumed that the predicted hardness of the first alloy was the same as the experimental result, and the result was added to a copy of the original dataset. The surrogate model

was then rebuilt, and the second experiment suggested was located where the AF was at a maximum. This procedure of continuously updating the surrogate model was repeated until a set number of ‘m’ compositions had been suggested, and those recommended compositions were subsequently fabricated and tested, with the experimental data being added to the original dataset, which constituted a single loop.

The active learning procedure was a crucial part of the workflow (Figure 3-7), and the alloys recommended by active learning were a part of the down-selected subset of alloys from the original dataset of alloys from the previous chapter.

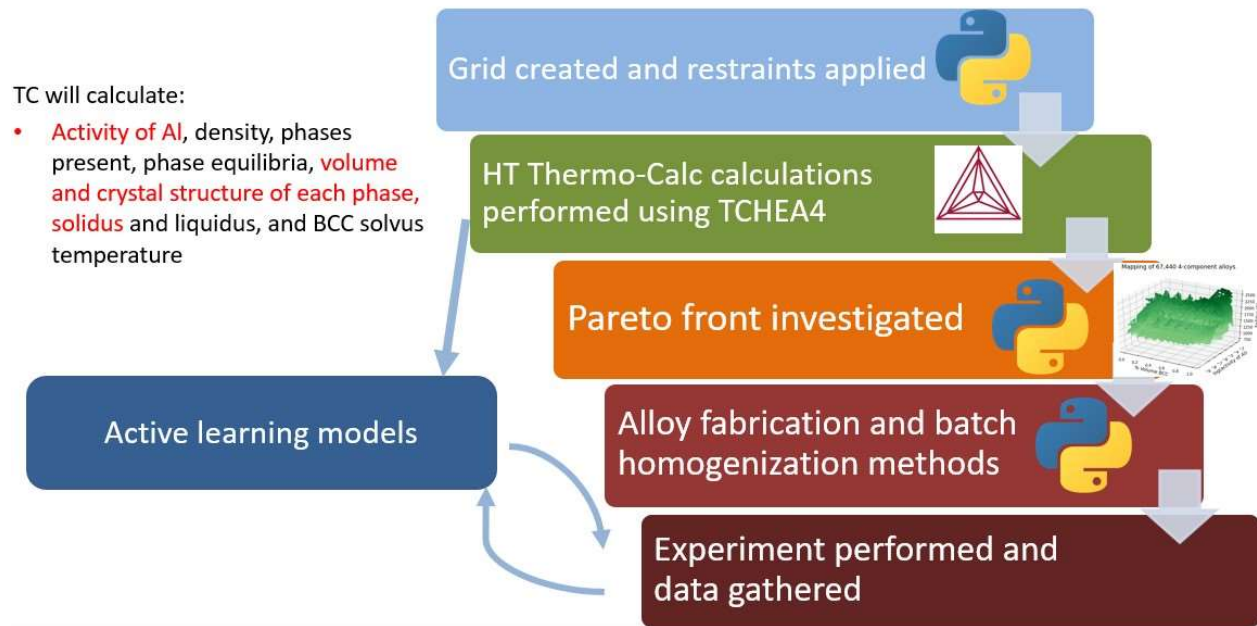


Figure 3-7. A workflow detailing the process from a grid of alloys potential RCCAs to a list of experiments, with the active learning loop a critical step in discovering novel alloy properties.

3.2.2 Experimental Methods

Alloy Fabrication Methods

All alloys fabricated in this active learning study were melted together from pure elements using a custom-built tri-arc melter with a 195-amp power source (XMT 350 CC/CV, Miller Electric, Appleton, WI, USA). Pure elements of aluminum granules (8-12 mm, 99.9% purity, Alfa Aesar, Ward Hill, MA, USA), titanium granules (1-10 mm, 99.99% purity excluding Na and K,

Alfa Aesar), vanadium foil (1 mm thick, 99.7% purity, Alfa Aesar), chromium chunks (2-3 mm, 99.995% purity, Alfa Aesar), niobium wire (1 mm diameter, 99.8% purity, Alfa Aesar), molybdenum wire (1 mm diameter, 99.94% purity, Alfa Aesar), hafnium wire (1 mm diameter, 99.95% purity excluding a nominal amount of 3% Zr, Alfa Aesar), and tungsten powder (average particle size of 21 microns, 99.9% purity, Alfa Aesar) were used. Pure elements with a total nominal mass of 5 grams before melting were weighed out on a high precision microbalance (ME36S, Sartorius AG, Goettingen, GER) to 4 significant figures.

After the charge material was weighed, the raw elements were evenly distributed and placed on a water-chilled copper hearth. The arc melter was then evacuated with a roughing pump (TRIVAC D2.5E, Leybold GmbH, Cologne, GER) for twenty minutes to allow the vacuum pressure to reach approximately 150 mTorr. The chamber was then filled with an inert cover gas of ultra-high purity argon (UHP Ar) (99.999% purity, Indiana Oxygen, Indianapolis, IN, USA). The evacuation/UHP Ar backfilling procedure was repeated three times. Upon completion of the backfilling procedure, the flow rate was monitored and controlled by a flow meter (Cole-Parmer, Vernon Hill, IL, USA) and kept constant at approximately 1400 mL/min.

All alloys were fabricated in a cover gas of UHP Ar to achieve a low oxygen concentration during melting. To further reduce the pO_2 , a Ti gettering furnace (OG120 gas purification furnace, Oxy-Gon Industries, Epsom, NH, USA) was utilized. Finally, a local getter of high purity zirconium was initially melted at the start of and during each experiment to remove residual oxygen left over from the backfilling procedure and inward diffusion of oxygen from the outside environment. An O_2 analyzer (Thermox CG1000, AMETEK Process Instruments, Berwyn, PA, USA) was utilized to record the oxygen concentration of the exhaust gases. After melting the Zr getter for O_2 purification, the charge material was melted into a single button and kept in the liquid state for approximately one minute, flipped and remelted 5 times to ensure homogeneity throughout the ingot.



Figure 3-8 A typical ingot shape after fabrication. The shape, presence of a shrinkage cavity, and luster of the final product is relevant for data storage purposes.

Upon completion of fabrication, the ingot, possessed a boule shape (Figure 3-8), which resembles a water droplet with a contact angle greater than 90° . Overall dimensions of alloy ingots ranged from approximately 6.5 to 8.5 mm in height and 13 to 16 mm in diameter. All alloys were weighed after fabrication to assess mass loss through evaporation, as both Al and Cr were prone to boiling at temperatures in excess of 2400°C .

Post-Fabrication Sample Preparation

Samples were sectioned into multiple pieces with a wire EDM (FX-20K, Mitsubishi Electric, Tokyo, JPN). Slices (2 mm) from near the center of the ingots were taken for mounting in conductive bakelite for hardness testing and microstructural evaluation. Cross-sectional samples were hot mounted with a compression mounting system (SimpliMet 4000, Buehler, Lake Bluff, IL, USA). Polishing was achieved by starting plane grinding with a 15 micron diamond platen (Allied High Tech Products, Inc., Rancho Dominguez, CA, USA), then a 9 micron diamond platen (Allied High Tech Products, Inc.), followed by fine polishing with a 6 micron diamond suspension in glycol (Allied High Tech Products, Inc) on a woven polishing cloth (Gold label, Allied High Tech Products, Inc) for approximately 5-10 minutes. The next polishing step was achieved by polishing with a 1 micron diamond suspension in glycol on a woven polishing cloth (Tech-cloth, Allied High Tech Products, Inc.) for approximately 5-10 minutes. Finally, the samples were polished for approximately 10 minutes on a non-woven, low nap porous polyurethane pad (Chem-Pol, Allied High Tech Products, Inc.) with a 0.04 micron colloidal silica suspension. The mounted

and polished specimens were then ultrasonicated in acetone for 5 minutes, and finally dried with forced air to remove residual particulates and surface contamination from the polishing procedure.

6 Cylindrical specimens approximately 4.67 to 4.82 mm in diameter were cut with a wire EDM (FX-20K, Mitsubishi Electric, Tokyo, JPN) from the ingot for compression testing. The ends of the sample were then cut down to a height of approximately 6.8 mm, and the faces of the samples were further smoothed by surface grinding to ensure flat, parallel surfaces. The samples were then shipped off to GE Research (1 Research Cir, Niskayuna, NY 12309) for compression testing to determine yield strength. The sample was preloaded with 5 lbf and a strain rate of 0.0017 in/s was applied until the sample failed, and peak load was recorded.

Sample Characterization

Upon completion of polishing, 16 hardness measurements were obtained on each sample. These measurements were taken by using an automatic micro-indenter (AMH43, Leco Corporation, St. Joseph, MI, USA) with 500 gram-force of load applied, and a dwell time of 13 seconds. The indents were arranged in a 4x4 square grid with each indentation spaced 300 microns from neighboring indentations. The location of the grid was chosen such that multiple microstructures (i.e., middle, side, and lower regions) are tested in order to fully sample the variation in hardness in a single ingot.

To verify phase a single-phase microstructure in the as-cast condition, X-ray diffraction (D2 Phaser diffractometer, Bruker, Billerica, MA, USA) was conducted using Cu K- α radiation ($\lambda = 0.154$ nm) with a scan rate of 0.23 degrees/s. To account for instrumental peak shifting, a standard of Nickel powder (99.8% purity, Alfa Aesar) was used, with a small amount placed on the surface of the sample.

Following XRD analysis, the alloys were examined in an SEM (NanoNova 450, FEI, Hillsboro, OR, USA) with a 15 kV accelerating voltage and a spot size of 5 microns, using BSE and SE imaging modes, and the elemental composition was verified using standardless EDS (AZtec software, Oxford Instruments, Abingdon, UK).

3.3 Results and Discussion

3.3.1 1st Iteration of Active Learning

In the first round of active learning, 6 alloys were recommended for hardness testing and subsequently fabricated by arc melting. The nominal compositions, compositions measured by EDS, predicted hardness and standard deviation of the prediction, mass loss of the ingot, predicted crystal structure, predicted BCC solvus temperature, solidus, and are tabulated in Table 3-1.

The HV data, along with the prediction and predicted standard deviation, are plotted in Figure 3-9a. Just in this first round, 3 alloys with higher hardness than the benchmark (AlMoNbTi) were found, and the experimental values were well within the predicted standard deviation. In Figure 3.9b, the XRD scans show a single set of BCC peaks for all alloys, despite microsegregation seen in most of the micrographs in Figure 3-10.

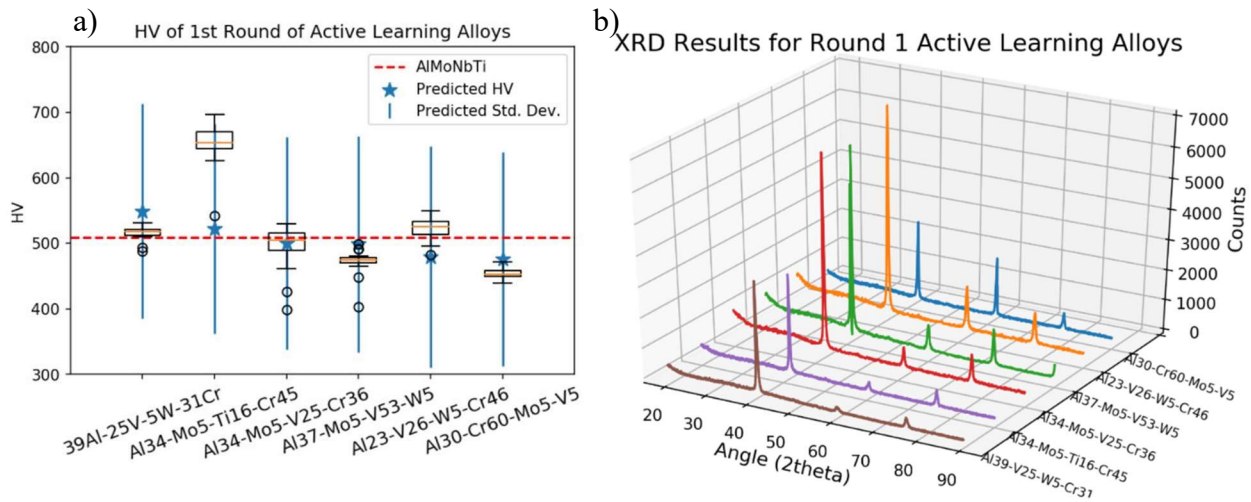


Figure 3-9. Results of HV testing compared to predictions for round 1 of active learning. b) XRD scans showing single set of BCC peaks for all alloys in round 1.

Despite the microsegregation, the spread of the data of the different alloys was relatively narrow. The hardness parity plot is given in Figure 3-11. The first-round results exhibited good agreement with the linear fit found for the other alloys in the database.

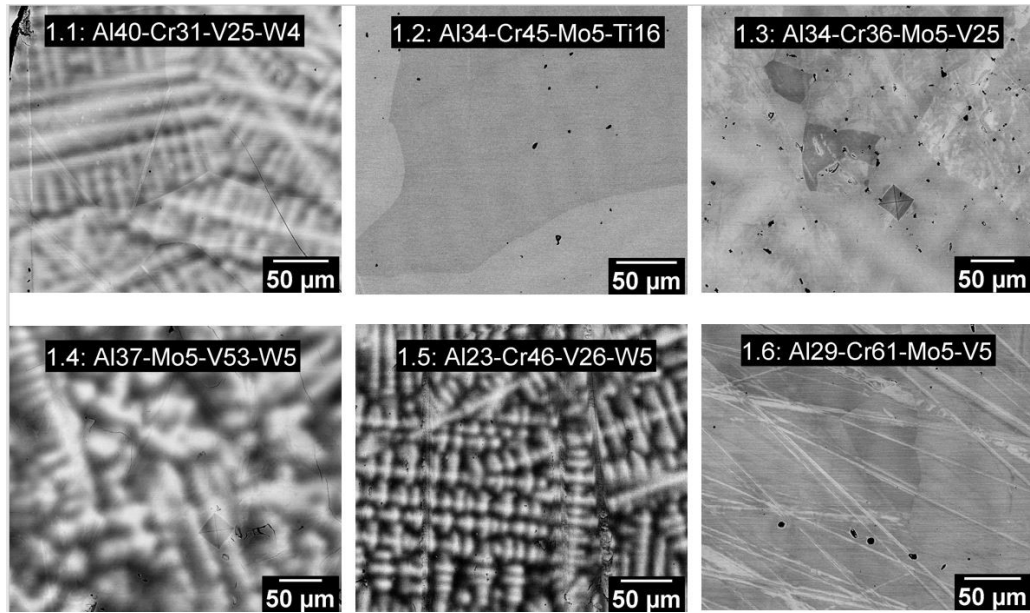


Figure 3-10. Polished micrographs taken with BSE imaging in the 1st round of active learning. Most of the alloys appear to have chemical microsegregation.

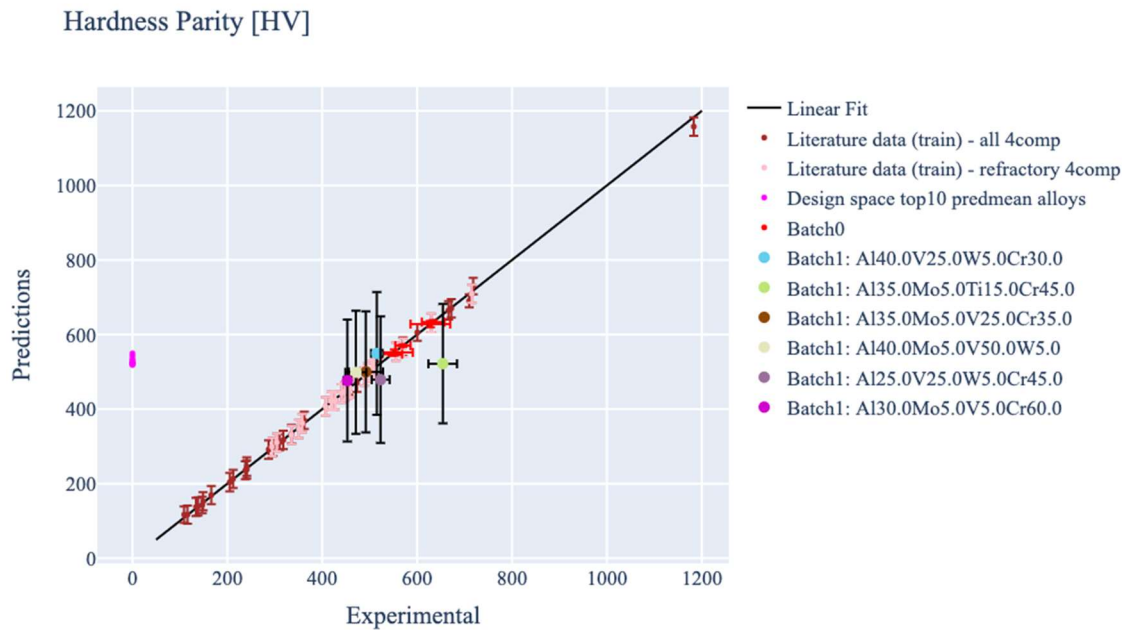


Figure 3-11 Hardness parity plot showing results of 1st round and comparison with literature data.

Table 3-1 Data for 1st round of active learning.

System	Nominal Comp.	Measured Comp.	Predicted HV (σ)	Measured HV (σ)	% mass loss	Al activity	Solidus °C	BCC solvus °C	Predicted Crystal Structure (Phase)
AlCrVW	Al40Cr30 V25W5	Al40Cr31 V25W4	549 (164)	515 (12)	2.7	.00036	1570	665	SS (BCC)
AlCrMoTi	Al35Cr45 Mo5Ti15	Al34Cr45 Mo5Ti16	521 (160)	654 (30)	2.8	.00012	1640	764	IM (B2)
AlCrMoV	Al35Cr35 Mo5V25	Al34Cr36 Mo5V25	500 (162)	492 (36)	2.0	.000202	1663	819	SS (BCC)
AlMoVW	Al40Mo5 V50W5	Al37Mo5 V53W5	498 (165)	471 (22)	3.05	.000169	1863	640	SS (BCC)
AlCrVW	Al25Cr45 V25W5	Al23Cr46 V26W5	479 (169)	523 (19)	3.4	8.3×10^{-5}	1777	891	SS (BCC)
AlCrMoV	Al30Cr60 Mo5V5	Al29Cr61 Mo5V5	476 (163)	453 (8)	1.6	.000174	1624	828	SS (BCC)

3.3.2 2nd Iteration of Active Learning

In the second round of active learning, 4 alloys were tested instead due to time and labor constraints. The same kind of data that was collected in Table 3-1 is tabulated in Table 3-2.

In the second round, all alloys tested were harder than AlMoNbTi, but the predicted mean HV were somewhat lower than the experimental mean (Figure 3.12a). However, the predicted standard deviation was in a similar range as the experimental data. Just like the previous active learning round, the XRD scans exhibit only BCC diffraction peaks. All the BSE micrographs of the alloys show significant chemical microsegregation. The hardness parity plot in Figure 3.14 shows more deviation than in the 1st round, but that may be due to exploration of unknown compositional space.

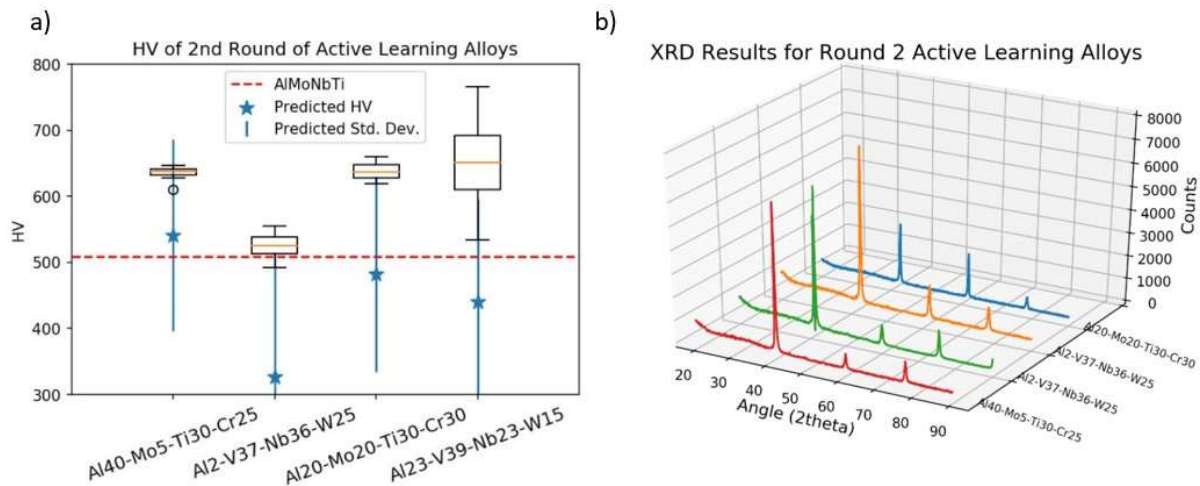


Figure 3-12. HV and XRD results for 2nd round of active learning. All alloys are harder than the benchmark, and the XRD scans only show 1 set of BCC peaks.

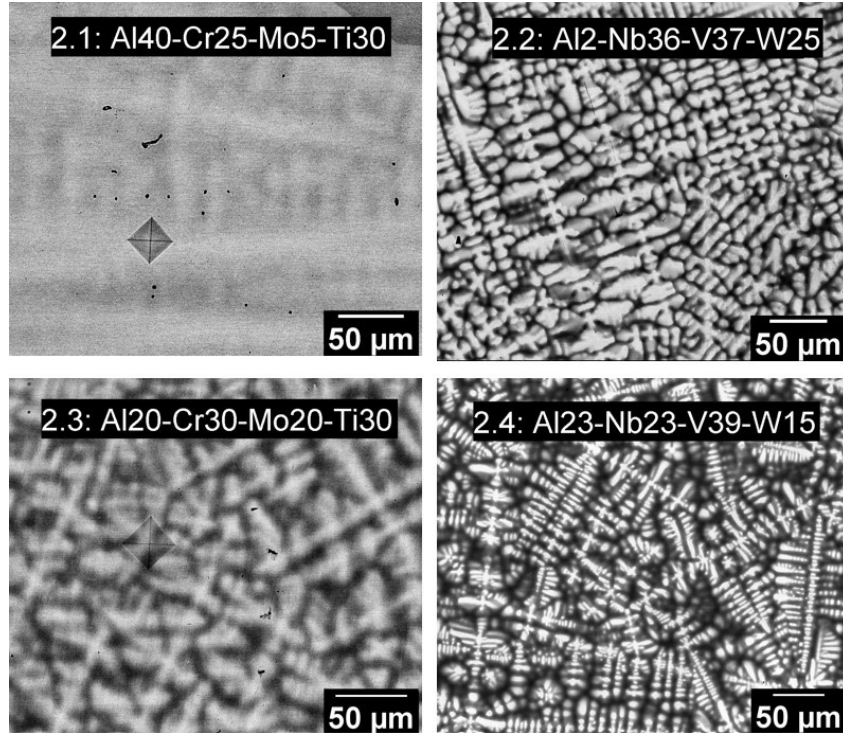


Figure 3-13. Polished micrographs taken with BSE imaging in the 2nd round of active learning.

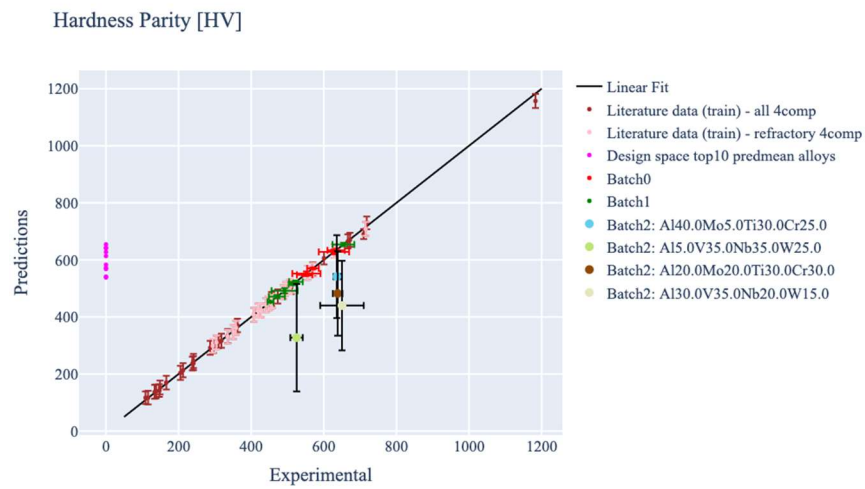


Figure 3-14 Hardness parity plot of the 2nd round which shows little agreement with the experimental hardness values.

Table 3-2 Data for 2nd round of active learning.

System	Nominal Comp.	Measured Comp.	Predicted HV (σ)	Measured HV (σ)	% mass loss	Al activity	Solidus °C	BCC solvus °C	Predicted Crystal Structure (Phase)
AlMoTiCr	Al40Cr25 Mo5Ti30	Al40Cr25 Mo5Ti30	541 (145)	636 (9)	9.8	0.000137	1593.29	975.98	IM (B2)
AlVNbW	Al5Nb35 V35W25	Al2Nb36 V37W25	327 (188)	525 (17)	3.3	1.63×10^{-6}	2137.62	149.47	SS (BCC)
AlMoTiCr	Al20Cr30 Mo20Ti30	Al20Mo20Ti3 0Cr30	482 (148)	638 (13)	1.8	9.90×10^{-6}	1790.18	933.15	IM (B2)
AlVNbW	Al30Nb20 V35W15	Al23Nb23V39 W15	439 (156)	650 (60)	4.3	5.83×10^{-5}	1907.54	439.65	SS (BCC)

3.3.3 3rd Iteration of Active Learning

Results for 3rd round of active learning are displayed in Table 3-3.

In the 3rd round of active learning, three out of the four alloys exhibited higher hardness than the benchmark (Figure 3-15) and XRD scans show good agreement with the previous round, The predictions were close to the experimental values. Micrographs of the alloys are shown in Figure 3-16 and two alloys exhibits substantial microsegregation (3.1 and 3.2) while 3.3 and 3.4 appear to exhibit very little chemical segregation, but this would need to be verified with further EDS analysis. Overall, the spread of the hardness results for an alloy are about the same as those in the previous rounds (see standard deviations) and the hardness parity plot (Figure 3-17) shows excellent agreement to the line of linear fit.

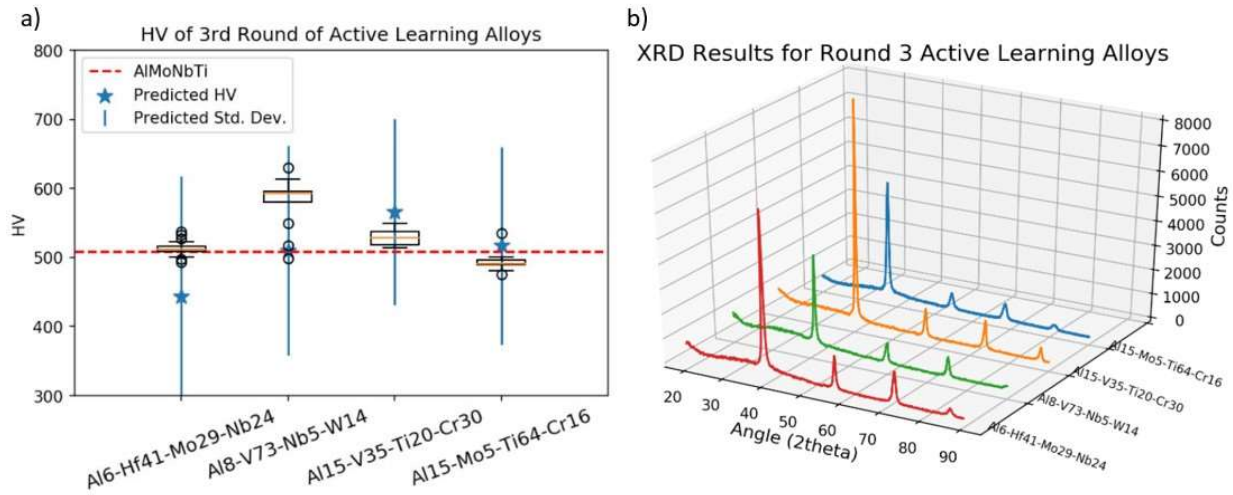


Figure 3-15 HV results and XRD scans for 3rd round of active learning

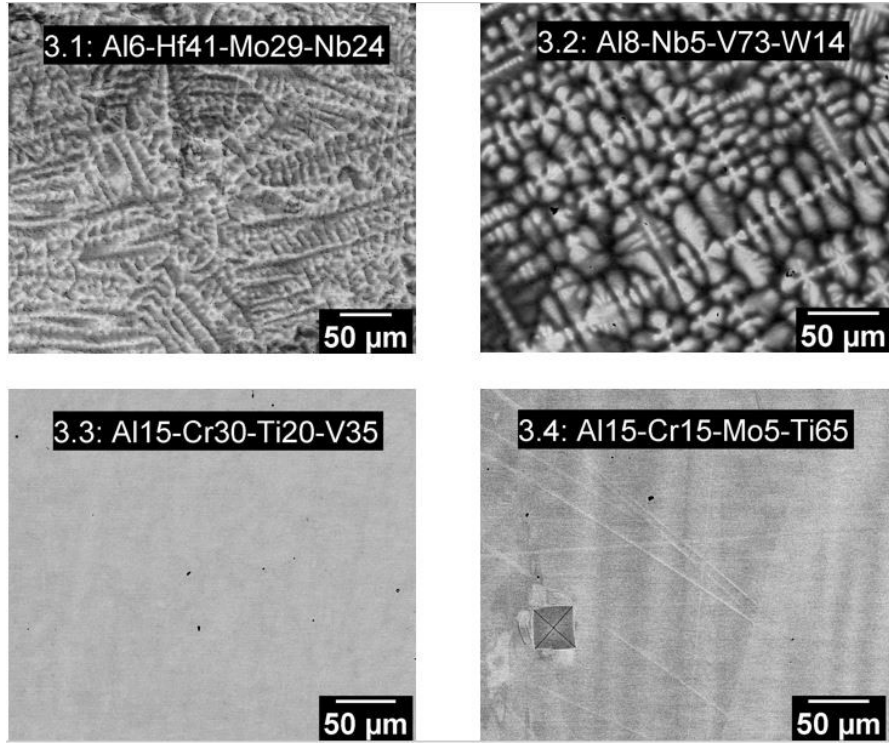


Figure 3-16. Polished micrographs taken with BSE imaging in the 3rd round of active learning.

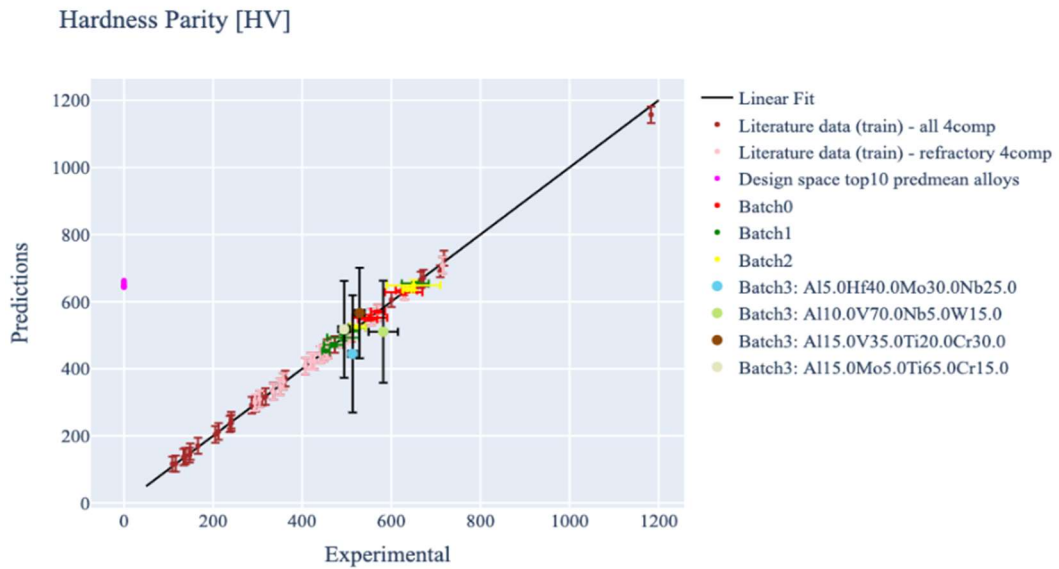


Figure 3-17. Hardness parity plot of the 3rd round showing excellent agreement with measured values.

Table 3-3 Data for 3rd round of active learning.

System	Nominal Comp.	Measured Comp.	Predicted HV (σ)	Measured HV (σ)	% mass loss	Al activity	Solidus °C	BCC solvus °C	Predicted Crystal Structure (Phase)
AlHfMoNb	Al5Hf40Mo30N25	Al6Hf4Mo29Nb24	444 (174)	513 (10)	0.38	2.55×10^{-6}	1853	989	SS (BCC)
AlNbVW	Al10Nb5V70W15	Al8Nb5V73W14	510 (152)	582 (33)	3.7	5.31×10^{-6}	1972	136	SS (BCC)
AlCrTiV	Al15Cr30Ti20V35	Al15Cr30Ti20V35	566 (135)	529(11)	0.8	1.63×10^{-5}	1554	734	IM (B2)
AlCrMoTi	Al15Cr15Mo5Ti65	Al15Cr15Mo5Ti65	517 (143)	394 (14)	2.7	2.24×10^{-6}	1701	799.46	IM (B2)

3.3.4 4th Iteration of Active Learning

Table 3-4. lists the data from this set of experiments.

In the 4th round of active learning, two out of the four alloys were harder than the benchmark, and the predictions again show excellent agreement with the results. HV and XRD data are shown in Figure 3-18 and the XRD scans again show a single set of BCC peaks. Microsegregation was observed for most of the alloys in round 4 (Figure 3-19), although alloy 4.2 showed no apparent microsegregation. Predictions also matched well with this round, as seen in the hardness parity plot (Figure 3-20).

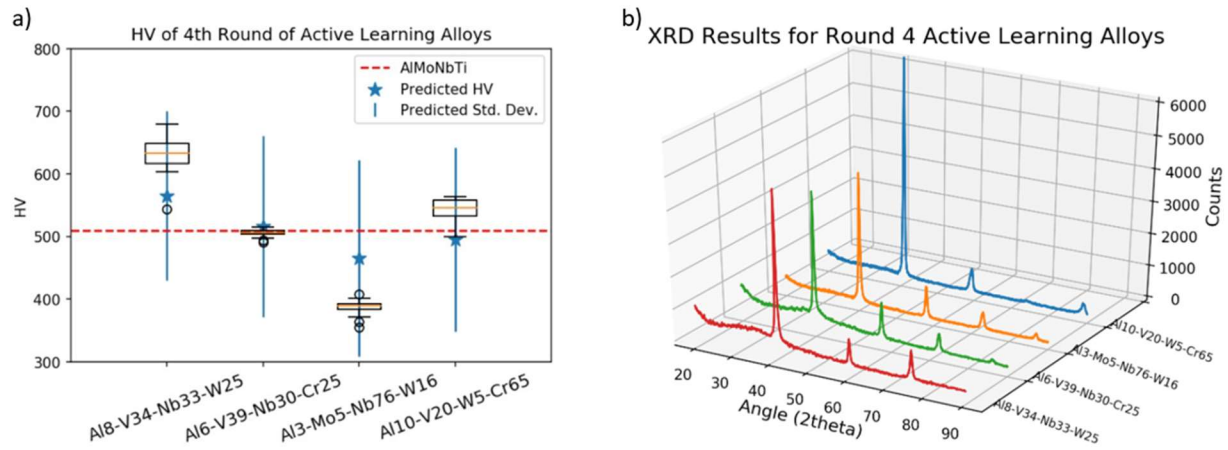


Figure 3-18. HV results and XRD scans for the 4th round of active learning.

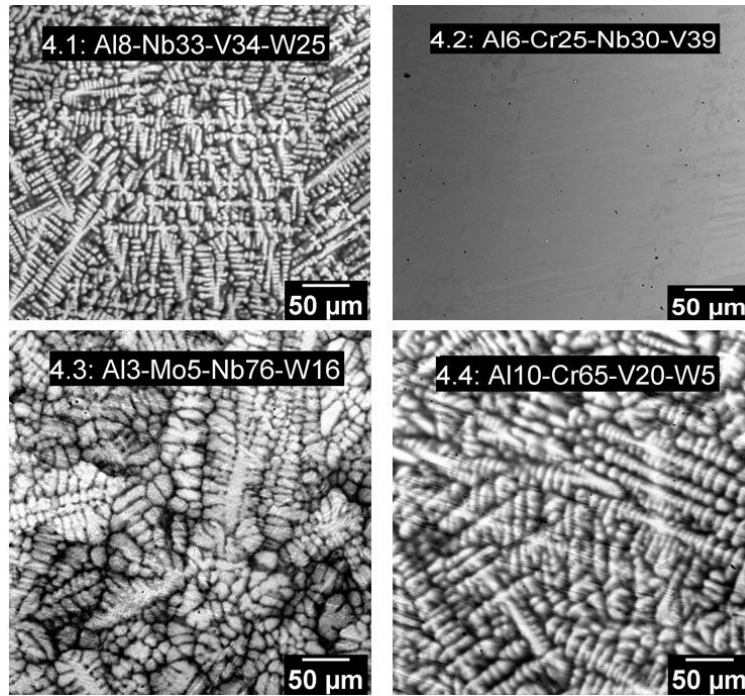


Figure 3-19. Polished micrographs taken with BSE imaging in the 4th round of active learning. Most of the alloys appear to have chemical microsegregation, except for 4.2.

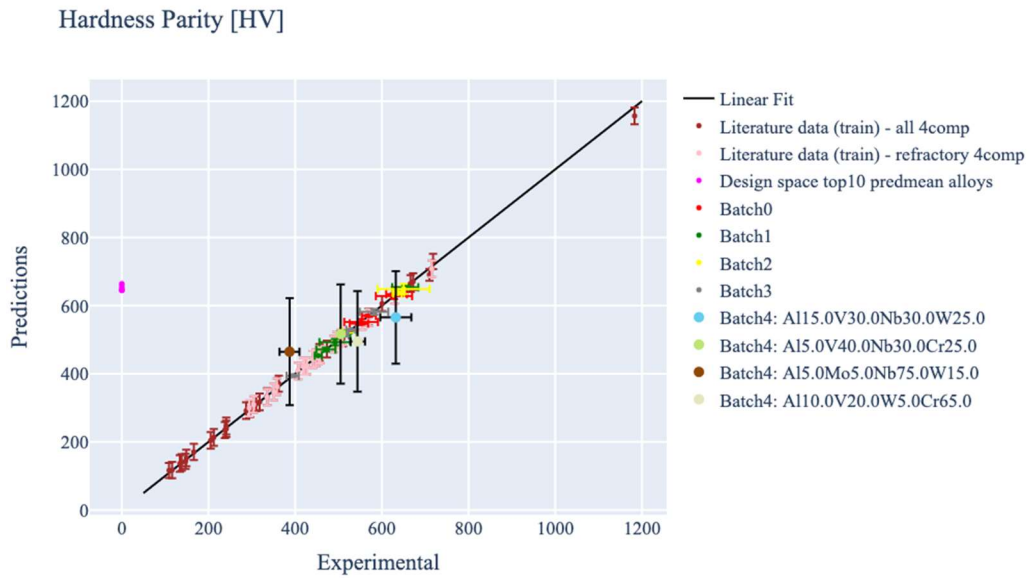


Figure 3-20. Hardness parity plot of the 4th round showing excellent agreement with the line of linear fit.

Table 3-4 Data for 4th round of active learning.

System	Nominal Comp.	Measured Comp.	Predicted HV (σ)	Measured HV (σ)	% mass loss	Al activity	Solidus °C	BCC solvus °C	Predicted Crystal Structure (Phase)
AlNbVW	Al15Nb30V30W25	Al8Nb33V34W25	565 (135)	632 (36)	7.31	1.11×10^{-5}	2068.32	305.22	SS (BCC)
AlCrNbV	Al5Cr25Nb30V40	Al6Cr25Nb30V39	516 (145)	505 (6.5)	0.21	1.60×10^{-6}	1738.19	938.65	SS (BCC)
AlMoNbW	Al5Mo5Nb75W15	Al3Mo5Nb76W16	464 (157)	387 (23)	3.4	3.09×10^{-6}	2451.53	279.42	SS (BCC)
AlCrVW	Al10Cr65V20W5	Al10Cr65V20W5	495 (147)	544 (17)	4.8	1.74×10^{-5}	1886.11	964.48	SS (BCC)

3.3.5 5th and final Iteration of Active Learning

Results for 5th round of active learning are displayed in Table 3-5.

In this round, the hardest alloy was discovered with the measured composition of Al₃₁V₃₂Nb₂₇W₁₀ (nominal Al₃₅V₃₀Nb₂₅W₁₀) and an HV of 690. More extensive analysis (such as TEM) of this alloy will be required to elucidate the causes of this high hardness, and an alloy from the same system (AlNbVW) should be compared to it for further understanding. The XRD scans show a single set of BCC peaks for all alloys. Besides the hardest alloy, the predictions for the other alloys were excellent.

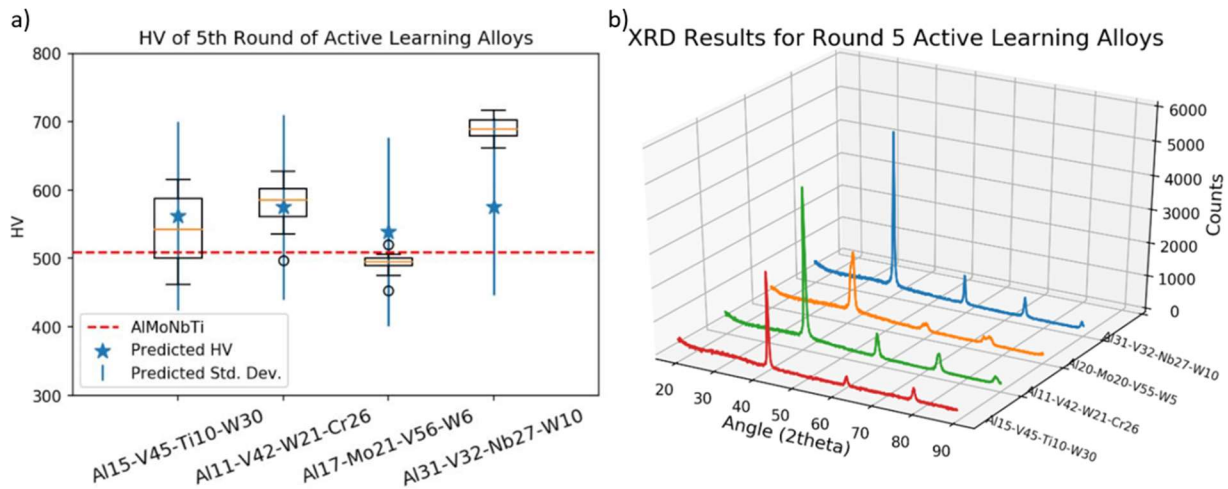


Figure 3-21 HV and XRD data from final round of active learning. Last alloy tested is the hardest out of all alloys tested in this loop.

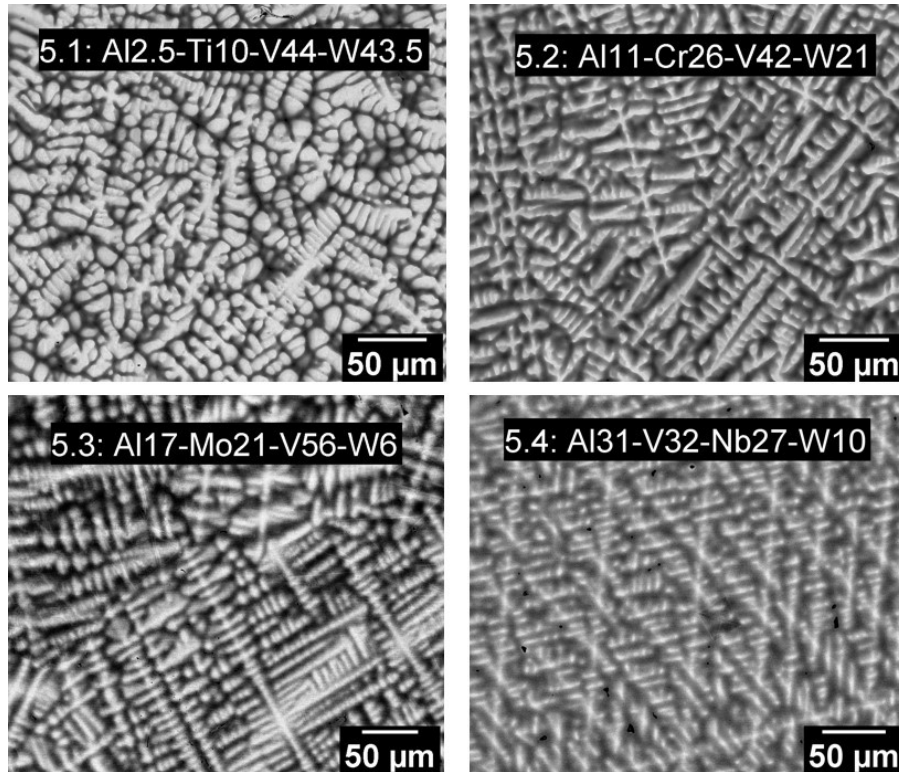


Figure 3-22. Polished micrographs taken with BSE imaging in the 5th round of active learning. All the alloys appear to exhibit chemical microsegregation.

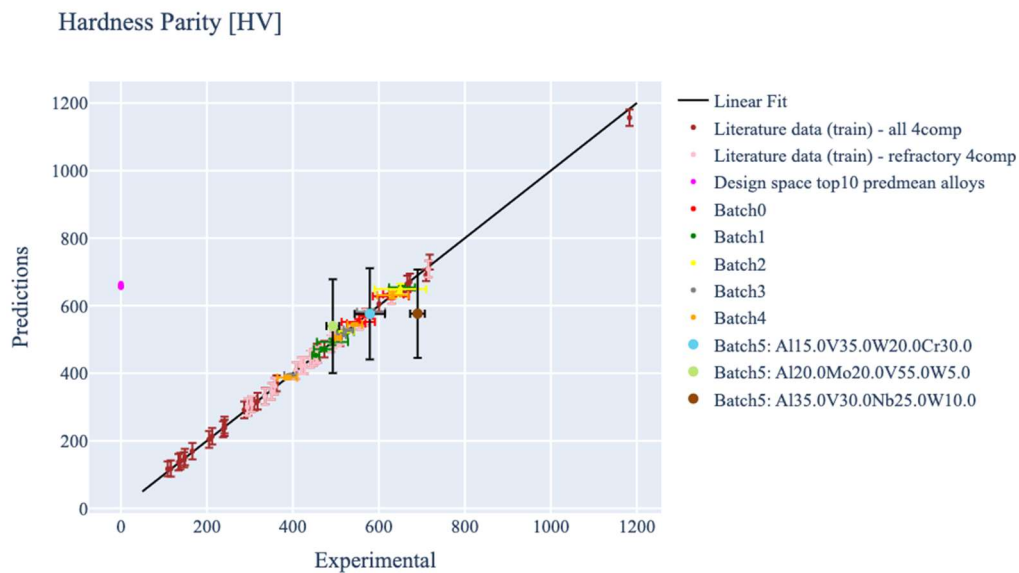


Figure 3-23 Hardness parity plot of the 5th round of active learning. Model appears to predict extremely HV well after only 5 iterations.

Table 3-5 Data for 5th round of active learning

System	Nominal Comp.	Measured Comp.	Predicted HV (σ)	Measured HV (σ)	% mass loss	Al activity	Solidus °C	BCC solvus °C	Predicted Crystal Structure (Phase)
AlVTiW	Al15Ti10 V45W30	Al2.5Ti10 V44W43.5	562 (138)	541 (50)	7.0	6.52×10^{-5}	1721	867	SS (BCC)
AlVWCr	Al15V35 W20Cr30	Al11Cr26 V42W21	575 (135)	579 (35)	11.7	2.27×10^{-5}	1939.09	857.04	SS (BCC)
AlMoVW	Al20Mo20 V55W5	Al17Mo21 V56W6	539 (138)	493 (15)	2.9	2.14×10^{-5}	2138.15	432.06	SS (BCC)
AlVNbW	Al35V30 Nb25W10	Al31V32 Nb27W10	576 (130)	690 (17)	4.3	0.000116	1829.9	532.55	SS (BCC)

3.3.6 Review of All Active Learning Iterations

When reviewing the data for all the active learning iterations, little progress was found in the accuracy of the model (Figure 3-24c). Also, the benchmark was 509 HV, and this procedure yielded 15 alloy compositions with HV values from 1 to 35% higher than the HV benchmark of 509. In Figure 3-24a, all XRD scans are compiled and it can be inferred that, at the resolution of XRD measurements, every alloy possessed a BCC-based structure with no intermetallic compounds detected by XRD analysis. In Figure 3-24b, it is seen that comparing the hardness to AlMoNbTi, the hardest alloy that fit our design space, there were 15 new, BCC-based alloys discovered with high hardness. Compared to CrNbTiW (HV: 630), the hardest 4 component alloy with refractory elements, there were 4 alloys that surpassed that benchmark. Figure 3-24c shows the difference between the model's predictions to the experimental value. From this plot, the model did not appreciably improve with each iteration.

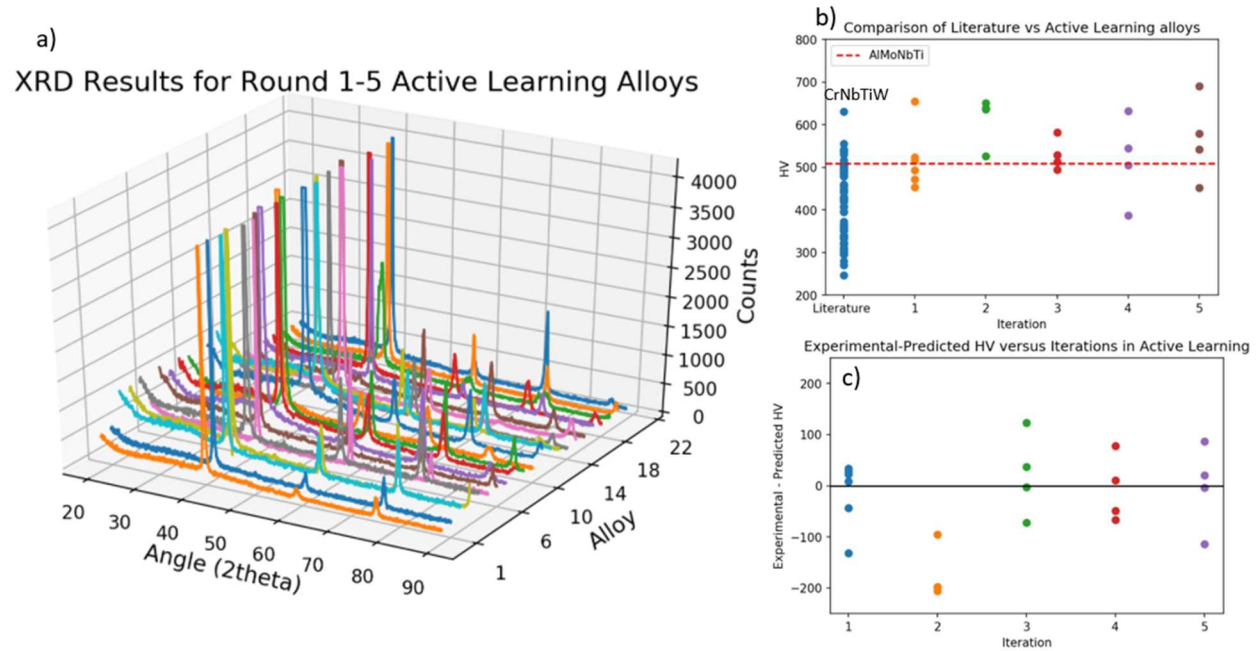


Figure 3-24 a) Compilation of XRD scans for all active learning alloys. b) Comparison of each iteration to the previous round and to literature values. Maximum is CrNbTiW with an HV of 630. c) Convergence of hardness predictions versus experimental values.

Figure 3-25 attempts to correlate the at% of an element to hardness. An analysis of the atomic percent of a single element reveals that no single element appears to have an appreciable effect on the Vickers hardness of an alloy. However it can be seen that in some alloys with over 50 at% of an element, there is a drop in the hardness (see Ti and Nb), which can support the theory of a high-entropy alloy exhibiting severe lattice distortion with near equimolar compositions.

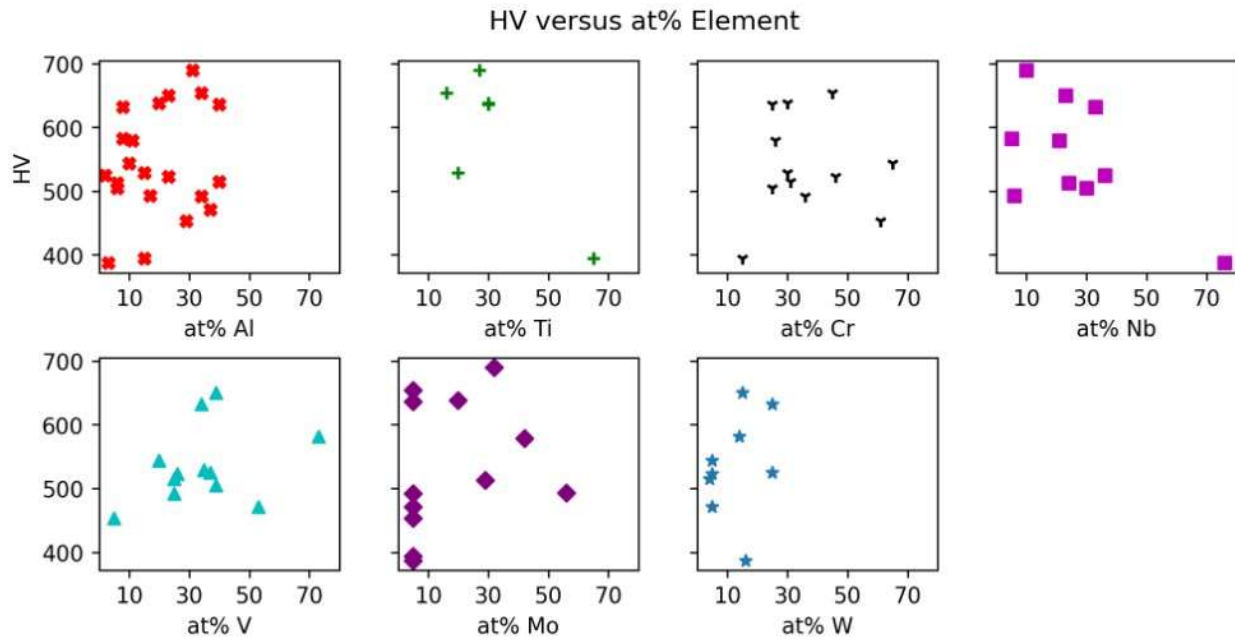


Figure 3-25 Plotting hardness versus at% of elements present in AL loop. No obvious trends are observed through these comparisons.

Figure 3-27 shows correlations between hardness, composition, and thermodynamic quantities such as solidus temperature and activity of Al. Correlations of hardness with a single element are shown, and it appears that there is a strong negative correlation with at% Nb and Ti, although this is likely skewed by alloys 4.3 and 3.4 for their high Nb and Ti contents, respectively. Interestingly, almost all quantities appear to have some effect on the lattice parameter (except hardness has little to no correlation with lattice parameter) as at% Ti, at% Nb, and at% W have strong positive correlations, while at% Al, Cr, and BCC solvus temperature have a medium negative correlation. Density, solidus, and entropy exhibit medium positive correlations with the lattice parameter.

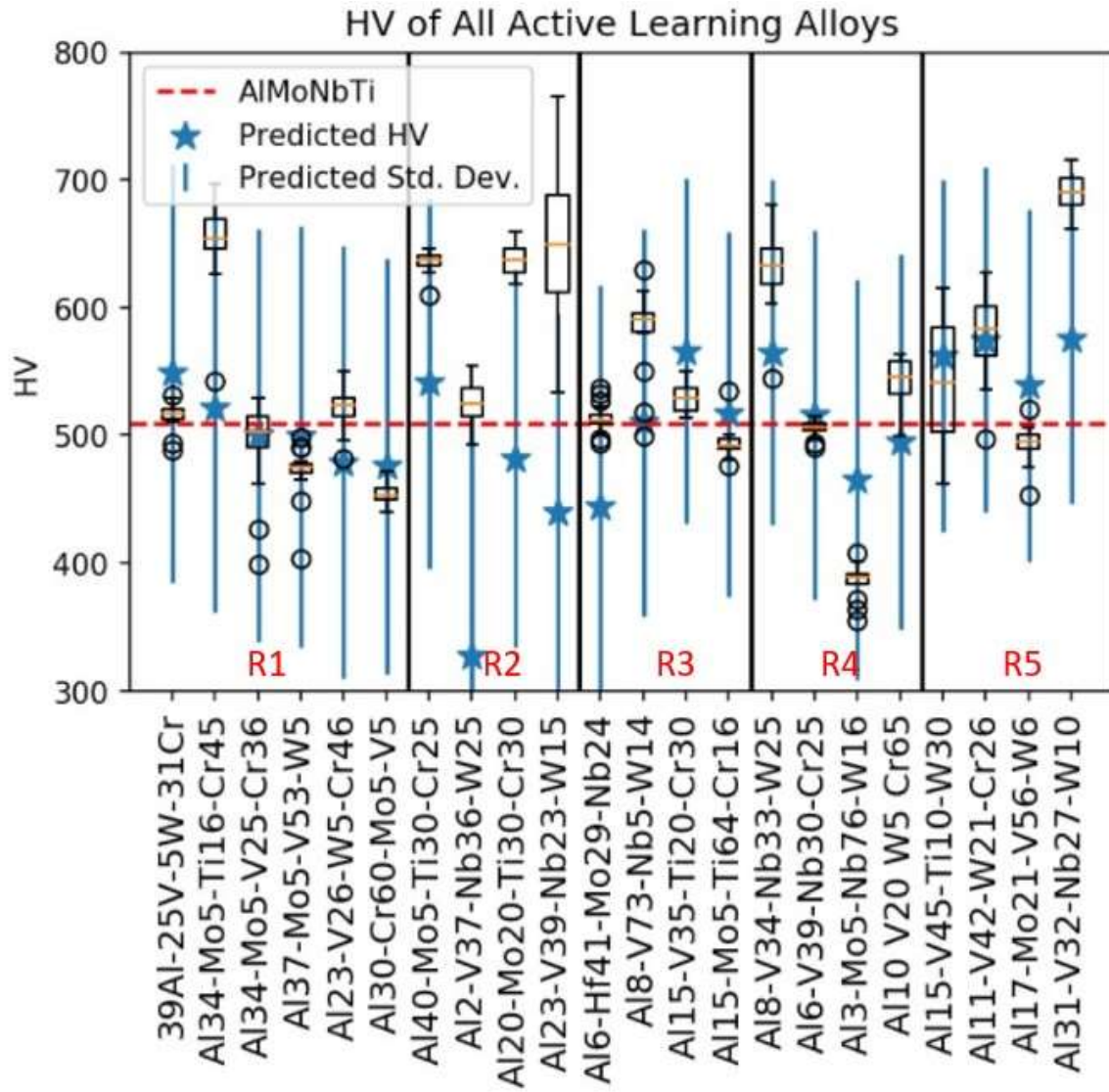


Figure 3-26. Compilation of hardness results from all iterations. Benchmark of AlMoNbTi is shown to have been passed by 15 alloys.

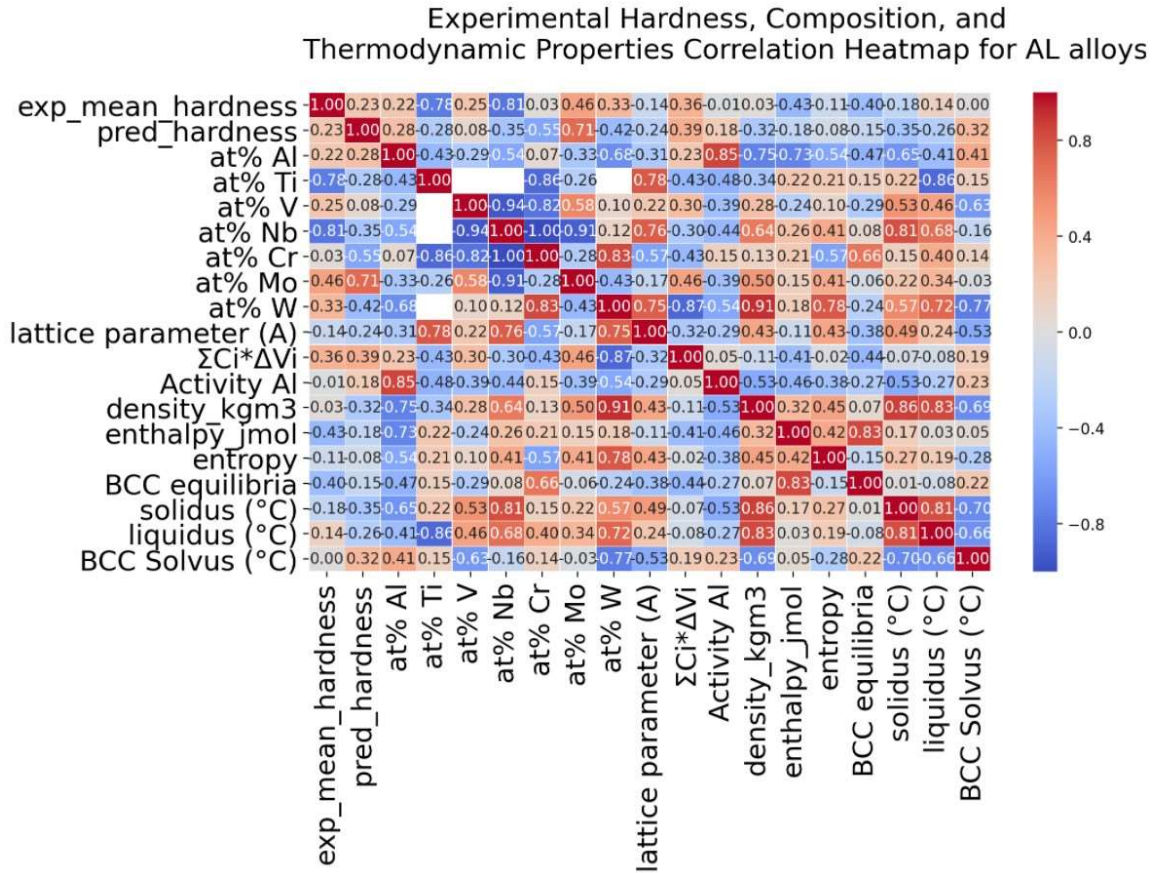


Figure 3-27. Correlation mapping of hardness versus composition and other thermodynamic properties.

3.3.7 Experimental and Theoretical Yield Strength

Three alloys from the top seven hardest were chosen for room temperature compression testing, which were the nominal compositions of Al35-V30-Nb25-W10, Al20-Cr30-Mo20-Ti30, and Al15-V30-Nb30-W25. The other alloys in the top seven hardest were disregarded for testing as they were either too brittle for sample preparation (such as Al35-Cr45-Mo5-Ti15 and Al40-Cr25-Mo5-Ti30) or is too compositionally close to another hard alloy (such as Al30-Nb20-W15-V35). The alloy exhibiting the highest yield stress (which is considered to be the peak stress as these alloys exhibited no ductility) is Al20-Cr30-Mo20-Ti30 (1209 MPa), followed by Al35-V30-Nb25-W10 (1019 MPa) and Al15-V30-Nb30-W25 (980 MPa), although all of the alloys tested failed catastrophically (best result is shown in Figure 3-28). Comparisons of RT yield strength with previously reported alloys are given in Figure 3-29, and it can be shown that there is slight

improvement over the strongest alloy in the design space of 4-component, single-phase, Al-bearing RCCAs (AlNbTaTi, YS of 1152 MPa).

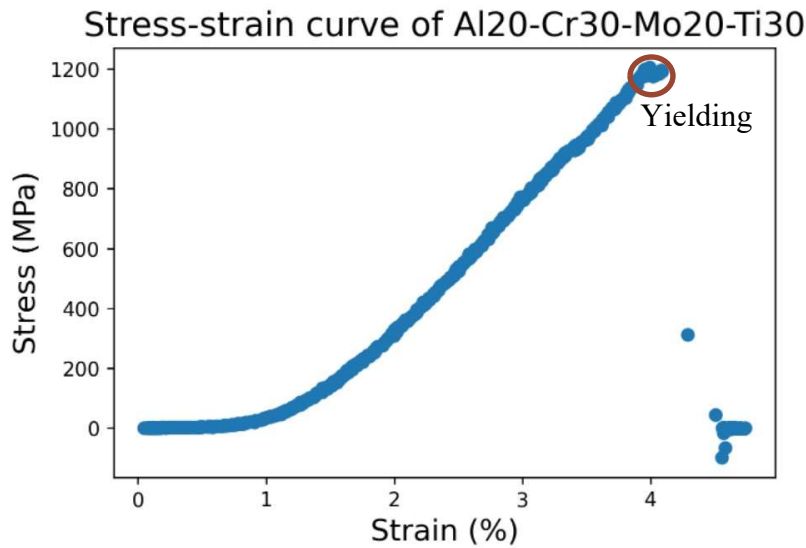


Figure 3-28. Stress strain curve of the strongest alloy evaluated by compression testing. The peak stress is recorded at the point of yielding and is circled.

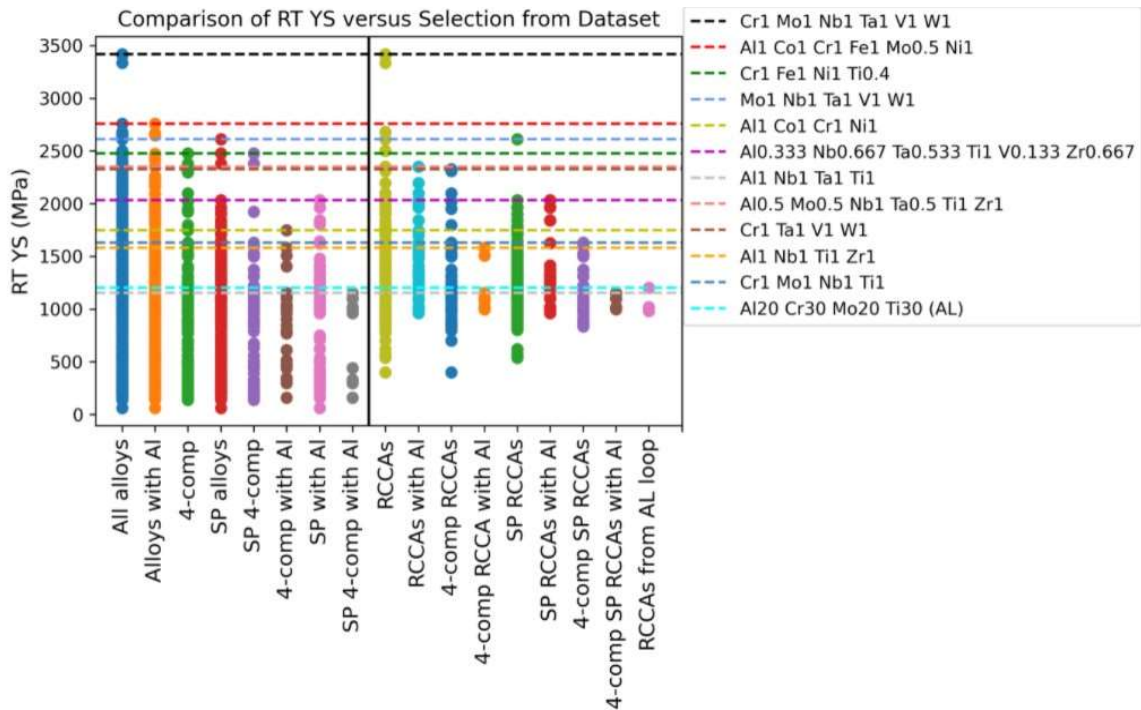


Figure 3-29. The RT yield strength comparisons of different categories of CCAs found in the literature. The three AL alloys tested are on the right-most column, and it is seen that a slight improvement over AlNbTaTi (YS: 1152 MPa) was accomplished.

The theoretical shear strength was calculated from DFT using the Curtin model of edge dislocations in BCC crystals^{44,45} with a strain rate of 0.01 s^{-1} at room temperature and $1000 \text{ }^{\circ}\text{C}$. A Taylor factor of 2.75 for BCC polycrystals was used to calculate the yield strength.^{46,47} Figure 3-30 shows the comparison between yield stress at room temperature, $1000 \text{ }^{\circ}\text{C}$, GP model predictions (same model as used for the active learning) and the experimental results of the three alloys evaluated by compression testing. Actual values of the shear and yield strength, temperature, Gaussian Process model predictions, and lattice parameters are provided in the appendix.

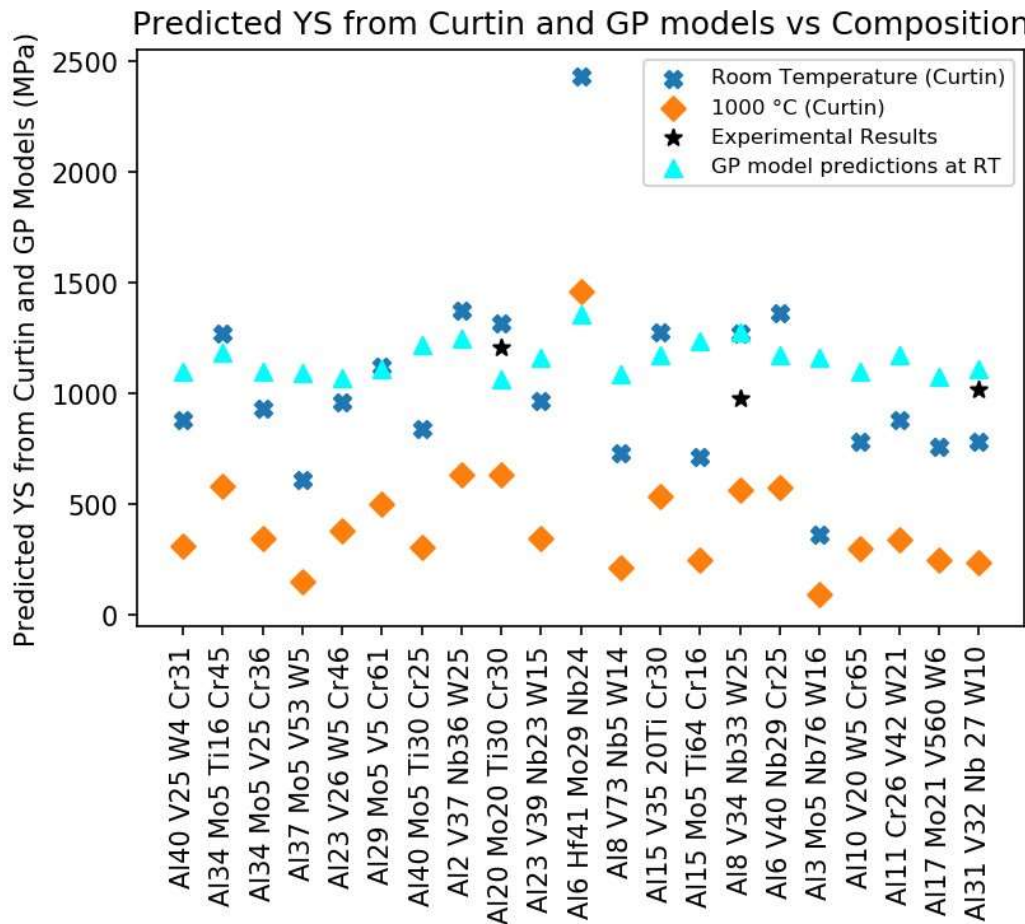


Figure 3-30. The predicted yield stresses at room temperature and $1000 \text{ }^{\circ}\text{C}$ are compared, and the experimental results are also shown in the plot. The actual yield strength of the three alloys show some agreement with the predicted values, and there the Al6-Hf41-Mo29-Nb24 exhibits anomalous high strength at both temperatures. Credit for DFT calculations goes to Dr. Dongsheng Wen and the GP model to Sharmila Karumuri.

From Figure 3-30, it can be shown that many of the alloys have similar predicted room temperature (from both GP and Curtin model) and high temperature strength compared to each other, with the exception of 6Al-41Hf-29Mo-24Nb, which exhibits extraordinarily high strengths

of 2436 MPa and 1461 MPa for room and high temperature conditions, respectively, and 1360 MPa from the GP model. This alloy had a hardness of 513 HV (Table 3-3), which was average compared to the other active learning alloys.

3.4 Conclusions

Active learning has already proven to be a useful tool in the field of materials science, and it has again played a crucial role in this study to rapidly discover high hardness alloys with minimal experimental trials. Through an amended Bayesian global optimization strategy that selected batches of alloys for experimental trials, 22 alloys were tested, and 15 of those alloys were harder than those previously reported in the literature that fit the design criteria of this work.

The model showed little to no improvement in predictions, and even though only 11 alloy systems were queried out the total of 84 in the design space, the active learning loop was capable of discovering multiple high hardness alloys. XRD and microstructural analyses do not reveal the formation of intermetallic compounds in the as-cast condition, although most exhibited some degree of microsegregation, and others did not. For example, alloys 1.1, 1.3, 1.4, 1.5, 2.1, 2.2, 2.3, 2.4, 3.1, 3.2, 4.1, 4.3, 4.4, 5.1, 5.2, 5.3, and 5.4 exhibited chemical microsegregation in the form of a dendritic microstructure. Alloys 1.2, 1.6, 3.3, 3.4, and 4.2 exhibited microstructures more representative of a single phase but point EDS analysis will be required to assess this. With this method of combining machine learning models with physics-based descriptors and the process of down-selecting Thermo-Calc generated alloys by filtering out those with undesirable properties, improved hardness, ranging from 1 to 35% over AlMoNbTi, was achieved.

Several trends can be found with composition with the lattice parameter, such as at% Ti, Nb, and W exhibited a notably strong positive correlation, while density, entropy of mixing, and solidus temperature exhibited a medium positive correlation. At% Al, Cr, and BCC solvus temperature exhibited a medium negative correlation. Further investigation of the AlNbVW (such as TEM analysis and comparison with another alloy of the same system, but lower hardness) and AlCrMoTi system are recommended for further study, as these two systems consistently resulted in high hardness.

Room temperature compression testing was also conducted, and the results reveal somewhat high strength, with a maximum yield strength of 1209 MPa (measured at fracture due to lack of ductility) for the composition of Al₂₀-Cr₃₀-Mo₂₀-Ti₃₀. Compared to the yield strength of other

alloys in the database with the selected design space, there is a small improvement over the alloy AlNbTaTi, which possesses a room temperature yield strength of 1152 MPa. Predicting the yield strength using the Curtin model and Gaussian Process model was also performed, and good agreement is found between the experimental and predicted results. An anomalously high strength alloy was predicted with the composition 6Al-41Hf-29Mo-24Nb was also found through the Curtin model predictions, and further characterization and experimentation of this alloy should be considered for future work.

4. CONCLUDING REMARKS AND FUTURE WORK

In summary of this thesis, thermodynamic properties of thousands of potential RCCAs were calculated, and machine learning was used to sample the design space for the purpose of replacing the current standard, Ni-based superalloys. RCCAs as a class of materials are still in their infancy, and there is a vast space of unexplored compositional territory. Efficient sampling of the compositional space is a daunting task, but a possible avenue for rapid exploration is proposed using the CALPHAD method, active learning, and rapid experimentation by maximizing low-fidelity data acquisition such as hardness. Of course, strength is only a small factor in determining if a material is suitable for desired harsh environments.

In the future, the alloys will require post-processing treatment to truly verify the single-phase microstructure predicted by Thermo-Calc, and a new set of hardness data should be gathered. The model should also account for the processing method. Also, only four-component alloys are considered in this work, and the number of possible alloys expand exponentially when just a single element is added to the mix, so another active learning loop with five component alloys may be considered. Furthermore, oxidation testing is needed to determine the RCCA mass gain over time, which is a crucial piece of information needed to balance between high strength with oxidation resistance.

For even more rapid experimental trials, high-throughput screening by the use of diffusion multiples should be explored. Diffusion multiples are an assembly of three or more alloys in contact and held at high temperature for an extended period of time to produce a compositional gradient. They have been proven to be an incredibly effective tool^{48–50} to map out the properties and microstructure of various systems, and this approach would undoubtedly accelerate RCCA discovery, as such experiments could elucidate the relationship between composition, mechanical properties, and oxidation behavior in a far more efficient manner than serial hardness testing.

Overall, the future of RCCAs is highly promising, and through efforts like the Materials Genome Initiative, and a toolbox involving machine learning and high-throughput experimentation, the discovery of suitable replacements of Ni-based superalloys within the next decade seems likely.

APPENDIX

Get_homogenization_window:

The `get_homogenization_window` function can be used to determine the homogenization temperature and number of cycles based off of the Scheil melting point, the solid solution solvus temperature, the homologous temperature (i.e., 60% of the solidus temperature), and the solidus temperature. This function, although very useful, was not used in this work as expediting the active learning process is the highest priority. However, future work will undoubtedly call for the need for homogenization treatments to verify single phase microstructures. Although this function can be used to calculate the temperatures and cycles for alloy homogenization, it does not provide the time for the homogenization treatment. If the user has not already calculated the mentioned parameters, the script will automatically calculate them and add them to a dictionary.

The contents of the dictionary were then evaluated, and the parameters were compared to determine the proper homogenization temperature and number of cycles. Minimum and maximum initial temperatures indicated the temperature window for homogenization in the first cycle, whereas minimum and maximum final temperatures indicate the homogenization window in the next cycle, if applicable. The number of stages was indicated, and a second homogenization cycle was recommended for low Scheil melting points to remove the low melting point phases.

In the case of a failure to calculate the Scheil melting point due to an internal error from the Thermo-Calc SDK, the program was used to determine if the homologous temperature was less than the solid solution solvus temperature. If it was true, then the minimum initial homogenization temperature was set equal to the solid solution solvus temperature and the maximum initial temperature was then set equal to the solidus temperature. In the case that the Scheil melting point and solid solution solvus temperature calculations failed, the minimum initial temperature was set equal to the homologous temperature and the maximum initial temperature was set equal to the solidus temperature. A single homogenization cycle was recommended for both cases.

In the case of a failure to calculate the solid solution solvus temperature, and with the homologous temperature less than the Scheil melting point, the minimum initial temperature was set equal to the homologous temperature. The maximum initial temperature was set equal to the

Scheil melting point, the minimum and maximum final was set equal the homologous and solidus temperatures, respectively, and a single homogenization treatment was recommended.

In the case where the solvus temperature was less than the homologous temperature, and with the homologous temperature less than the Scheil melting point, the minimum initial and minimum final temperatures was set to the homologous temperature, the maximum initial temperature was set to the Scheil melting point, the maximum final temperature was set to the solidus temperature, and a single homogenization treatment was recommended.

In the case where the solvus temperature was greater than the homologous temperatures, and less than the Scheil melting point, the minimum initial temperature was set to the solvus. The maximum initial homogenization treatment was set to the Scheil melting point, and a single homogenization cycle was recommended.

In the case where the homologous temperature was less than the Scheil melting point, and with the Scheil melting point less than the solid solution solvus temperature, the minimum and maximum initial temperatures were set to the homologous temperature and the Scheil melting point, respectively. The minimum final temperature and the maximum final temperature were set to the solid solution solvus temperature and the solidus temperature, respectively, and a double heat treatment was recommended.

In the case where the Scheil melting point was less than both the homologous and solvus temperature, the minimum and maximum initial temperatures were set to the Scheil melting point to prevent the melting of a low-melting-point phase. After the initial cycle, a second cycle was recommended between the minimum and maximum temperatures of the solvus and solidus temperatures, respectively.

Finally, if the Scheil melting point was lower than both the homologous and solvus temperatures, and the homologous temperature was less than the solvus temperature, the minimum and maximum initial temperatures were set to the Scheil melting point. The minimum and maximum final homogenization temperatures were set to the homologous and solidus temperatures, respectively, and a double homogenization cycle was recommended.

Table 4-1. The compositions, lattice parameters, predicted shear strength found from the Curtin model, yield strength found by multiplying by a Taylor factor of 2.75 for BCC polycrystals, GP model predictions, and experimental yield strength, if measured for AL alloys.

Composition (at%)	Lattice Parameter (Å)	τ_y (MPa) at RT	τ_y (MPa) at 1000 °C	Yield stress (MPa) at RT	Yield stress (MPa) at 1000 °C	GP model YS (MPa) at RT	Experimental YS (MPa)
Al40-Cr31-V25-W4	3.044	320.81	113.97	882.32	313.4	1100.7	
Al34-Mo5-Ti16-Cr45	3.041	462.33	211.78	1271.4	582.4	1183.3	
Al34-Mo5-V25-Cr36	3.014	338.25	126.04	930.19	346.61	1101.3	
Al37-Mo5-V53-W5	3.082	222.86	54.65	612.86	150.29	1094.8	
Al23-V26-W5-Cr46	2.992	349.13	138.49	960.1	380.85	1071.8	
Al29-Mo5-V5-Cr61	3.124	409.07	182.46	1124.94	501.77	1109.5	
Al40-Mo5-Ti30-Cr25	3.115	305.93	110.62	841.3	304.2	1217.5	
Al2-V37-Nb36-W25	3.179	500.93	230.11	1377.56	632.86	1250.5	
Al20-Mo20-Ti30-Cr30	3.113	478.59	230.13	1316.12	632.86	1066.9	1209
Al23-V39-Nb23-W15	3.144	352.56	125.94	969.54	346.34	1163.5	
Al6-Hf41-Mo29-Nb24	3.359	885.86	531.49	2436.12	1461.6	1360.6	
Al8-V73-Nb5-W14	3.084	266.7	78.62	733.43	216.2	1087.8	
Al15-V35-Ti20-Cr30	3.047	464.09	194.93	1276.25	536.06	1173.9	
Al15-Mo5-Ti64-Cr16	3.19	260.4	89.66	716.1	246.56	1238.8	
Al8-V34-Nb33-W25	3.177	462.38	205.31	1271.55	564.6	1279.7	980
Al6-V40-Nb29-Cr25	3.126	496.46	210.12	1365.27	577.83	1172.2	
Al3-Mo5-Nb76-W16	3.272	132.65	33.14	364.79	91.14	1162.6	
Al10-V20-W5-Cr65	2.947	285.23	110.18	784.4	303.0	1100.5	
Al11-Cr26-V42-W21	3.036	320.36	124.68	881.0	342.87	1175.1	
Al17-Mo21-V56-W6	3.082	277.42	89.86	762.9	247.12	1074.0	
Al31-V32-Nb27-W10	3.172	284.78	86.82	783.15	283.76	1112.3	1019

REFERENCES

1. Reed, R. C. *The Superalloys as High-Temperature Materials. The Superalloys* (2006).
2. Superalloys, C. Superalloys for gas turbine engines. *Introd. to Aerosp. Mater.* 251–267 (2012) doi:10.1533/9780857095152.251.
3. Sims, C. T. A History of Superalloy Metallurgy for Superalloy Metallurgists. 399–419.
4. Stott, F. H., Wood, G. C. & Stringer, J. The influence of alloying elements on the development and maintenance of protective scales. *Oxid. Met.* **44**, 113–145 (1995).
5. Sheikh, S., Gan, L., Montero, X., Murakami, H. & Guo, S. Forming protective alumina scale for ductile refractory high-entropy alloys via aluminizing. *Intermetallics* **123**, 106838 (2020).
6. Schneibel, J. H. *et al.* Symposium ‘Beyond nickel-base superalloys’. *Metall. Mater. Trans. A Phys. Metall. Mater. Sci.* **36**, 481 (2005).
7. Senkov, O. N., Gorsse, S. & Miracle, D. B. High temperature strength of refractory complex concentrated alloys. *Acta Mater.* **175**, 394–405 (2019).
8. Senkov, O. N., Miracle, D. B., Chaput, K. J. & Couzinie, J. P. Development and exploration of refractory high entropy alloys - A review. *J. Mater. Res.* **33**, 3092–3128 (2018).
9. Miracle, D. B. & Senkov, O. N. A critical review of high entropy alloys and related concepts. *Acta Mater.* **122**, 448–511 (2017).
10. Snead, L. L., Hoelzer, D. T., Rieth, M. & Nemith, A. A. N. *Chapter 13 - Refractory Alloys: Vanadium, Niobium, Molybdenum, Tungsten. Structural Alloys for Nuclear Energy Applications* (Elsevier Inc., 2019). doi:10.1016/B978-0-12-397046-6.00013-7.
11. Murty, B. S., Yeh, J. W., Ranganathan, S. & Bhattacharjee, P. P. High-entropy alloys: basic concepts. *High-Entropy Alloy*. 13–30 (2019) doi:10.1016/b978-0-12-816067-1.00002-3.
12. Gorr, B. *et al.* A new strategy to intrinsically protect refractory metal based alloys at ultra high temperatures. *Corros. Sci.* **166**, (2020).
13. Srikanth, M., Raja Annamalai, A., Muthuchamy, A. & Jen, C. P. A review of the latest developments in the field of refractory high-entropy alloys. *Crystals* **11**, 1–15 (2021).
14. Gorsse, S., Miracle, D. B. & Senkov, O. N. Mapping the world of complex concentrated alloys. *Acta Mater.* **135**, 177–187 (2017).
15. Lo, K. C., Chang, Y. J., Murakami, H., Yeh, J. W. & Yeh, A. C. An oxidation resistant refractory high entropy alloy protected by CrTaO₄-based oxide. *Sci. Rep.* **9**, 3–4 (2019).

16. Kelvin, Lord, Feynman, R., Computational, I. & Engineering, M. Alloy design in the 21st century: ICME, materials genome, and artificial intelligence strategies 5.1. (2019) doi:10.1016/B978-0-12-816067-1.00005-9.
17. Gröbner, J. & Schmid-Fetzer, R. Thermodynamic modeling of the Al-Ta system. *Scr. Mater.* **63**, 674–679 (2010).
18. Wang, H., Reed, R. C., Gebelin, J. C. & Warnken, N. On the modelling of the point defects in the ordered B2 phase of the Ti-Al system: Combining CALPHAD with first-principles calculations. *Calphad Comput. Coupling Phase Diagrams Thermochem.* **39**, 21–26 (2012).
19. Durga, A., Hari Kumar, K. C. & Murty, B. S. Phase formation in equiatomic high entropy alloys: CALPHAD approach and experimental studies. *Trans. Indian Inst. Met.* **65**, 375–380 (2012).
20. Lee, J. W. *et al.* A machine-learning-based alloy design platform that enables both forward and inverse predictions for thermo-mechanically controlled processed (TMCP) steel alloys. *Sci. Rep.* **11**, 1–18 (2021).
21. Wen, C. *et al.* Machine learning assisted design of high entropy alloys with desired property. *Acta Mater.* **170**, 109–117 (2019).
22. Li, R., Xie, L., Wang, W. Y., Liaw, P. K. & Zhang, Y. High-Throughput Calculations for High-Entropy Alloys: A Brief Review. *Front. Mater.* **7**, 1–12 (2020).
23. Pilania, G. Machine learning in materials science: From explainable predictions to autonomous design. *Comput. Mater. Sci.* **193**, 110360 (2021).
24. Lookman, T., Balachandran, P. V., Xue, D. & Yuan, R. Active learning in materials science with emphasis on adaptive sampling using uncertainties for targeted design. *npj Comput. Mater.* **5**, (2019).
25. Manzoni, A. M. *et al.* On the path to optimizing the Al-Co-Cr-Cu-Fe-Ni-Ti high entropy alloy family for high temperature applications. *Entropy* **18**, (2016).
26. Szymański, P., Markowicz, M. & Mikiciuk-Olasik, E. Adaptation of high-throughput screening in drug discovery-toxicological screening tests. *Int. J. Mol. Sci.* **13**, 427–452 (2012).
27. Sverchkov, Y. & Craven, M. A review of active learning approaches to experimental design for uncovering biological networks. 1–26 (2017).
28. Pasolli, E. & Melgani, F. GAUSSIAN PROCESS REGRESSION WITHIN AN ACTIVE LEARNING SCHEME Edoardo Pasolli and Farid Melgani Dept . of Information Engineering and Computer Science , Univ . of Trento , Italy. 3574–3577 (2011).
29. Titus, M. S. & Hernandez, A. M. pyTCplotter. 7 (2022).

30. Kubaschewski, O. & Heymer, G. The thermodynamics of the chromium-iron system. *Acta Metall.* **8**, 416–423 (1960).
31. Wang, C. P. *et al.* Intermetallics Experimental investigation and thermodynamic calculation of the phase equilibria in the Co – Mo – W system. *Intermetallics* **17**, 642–650 (2009).
32. Peterlongo, A., Miotello, A. & Kelly, R. Laser-pulse sputtering of aluminum: Vaporization, boiling, superheating, and gas-dynamic effects. **50**, (1994).
33. Maiti, S. & Steurer, W. Acta Materialia Structural-disorder and its effect on mechanical properties in single- phase TaNbHfZr high-entropy alloy. *Acta Mater.* **106**, 87–97 (2016).
34. Wang, R. *et al.* Novel metastable engineering in single-phase high-entropy alloy. *Mater. Des.* **162**, 256–262 (2019).
35. Murray, J., Peruzzi, A. & Abriata, J. P. The Al-Zr (aluminum-zirconium) system. *J. Phase Equilibria* **13**, 277–291 (1992).
36. Chatain, S., Guéneau, C., Labroche, D., Rogez, J. & Dugne, O. Thermodynamic assessment of the Al-Hf binary system. *J. Phase Equilibria* **24**, 122–131 (2003).
37. Mahdouk, K. & Gachon, J. C. Thermodynamic investigation of the aluminum-chromium system. *J. Phase Equilibria* **21**, 157–166 (2000).
38. Wan, H. *et al.* A Novel Method of Fabricating Al-V Intermetallic Alloy through Electrode Heating. (2019).
39. Bose, I. & Mahapatra, R. K. Business data mining Ð a machine learning perspective. **39**, 211–225 (2001).
40. Rammer, W. & Seidl, R. Harnessing Deep Learning in Ecology : An Example Predicting Bark Beetle Outbreaks. **10**, 1–9 (2019).
41. Farnell, M. S., McClure, Z. D., Tripathi, S. & Strachan, A. Modeling environment-dependent atomic-level properties in complex-concentrated alloys. *J. Chem. Phys.* **156**, 114102 (2022).
42. Cahoon, J. R. The Determination of Yield Strength From Hardness Measurements. (1979).
43. Borg, C. K. H. *et al.* Expanded dataset of mechanical properties and observed phases of multi-principal element alloys. 1–6 (2020) doi:10.1038/s41597-020-00768-9.
44. Maresca, F. & Curtin, W. A. Mechanistic origin of high strength in refractory BCC high entropy alloys up to 1900K. *Acta Mater.* **182**, 235–249 (2020).
45. Wen, D. pySSpredict. 8 (2020).
46. Busby, J. T., Hash, M. C. & Was, G. S. The relationship between hardness and yield stress in irradiated austenitic and ferritic steels. *J. Nucl. Mater.* **336**, 267–278 (2005).

47. Rao, S. I., Woodward, C., Akdim, B., Senkov, O. N. & Miracle, D. Theory of solid solution strengthening of BCC Chemically Complex Alloys. *Acta Mater.* **209**, 116758 (2021).
48. Zhao, J., Jackson, M. R. & Peluso, L. A. Determination of the Nb – Cr – Si phase diagram using diffusion multiples. **51**, 6395–6405 (2003).
49. Zhao, J. C., Zheng, X. & Cahill, D. G. High-throughput diffusion multiples. *Mater. Today* **8**, 28–37 (2005).
50. Zhao, J. C., Jackson, M. R. & Peluso, L. A. Mapping of the Nb-Ti-Si phase diagram using diffusion multiples. *Mater. Sci. Eng. A* **372**, 21–27 (2004).